

Electron scattering at 4° with energies of 4.5–20 GeV*

S. Stein,[†] W. B. Atwood, E. D. Bloom, R. L. A. Cottrell, H. DeStaabler, C. L. Jordan,[‡] H. G. Piel,[§] C. Y. Prescott, R. Siemann, and R. E. Taylor

Stanford Linear Accelerator Center, Stanford University, Stanford, California 94305

(Received 23 January 1975)

This paper presents the results of the analysis of a single-arm inelastic-electron-scattering experiment at an angle of 4° . We present data on the turnon of scaling in the low- q^2 region $0.1 < q^2 < 1.8$, the neutron-proton comparison at large values of the scaling variable ω , resonance excitation, and the shadowing in scattering from heavy nuclei.

From the time of Rutherford's analysis of α particle scattering, the scattering of charged particles has provided a probe with which we are still learning about the structure of matter. The experimental observation¹ of large, almost point-like, cross sections in electron scattering has prompted much discussion of constituent models of the nucleon, notably the parton model. The prediction of Bjorken² regarding scaling behavior for nucleon structure functions was also approximately verified, and at rather small values of q^2 , the four-momentum transfer. The present experiment, which measures electron scattering at an angle of 4° for various incident energies, was designed to investigate the structure functions νW_2 for the proton and neutron for values of q^2 smaller than those for which scaling has already been observed. In addition to this study of the turn-on of scaling, the study of the ratio of neutron and proton scattering at large values of the scaling variable $\omega = 2M\nu/q^2$ is of interest.

Inelastic scattering can be considered as photoproduction by off-mass-shell photons. The total photoproduction cross section is connected in a simple way with the inelastic scattering of electrons in the limit $q^2 \rightarrow 0$. In the present experiment, data for values of q^2 from 0.1 to 1.8 $(\text{GeV}/c)^2$ provide some opportunities to study how photoproduction is modified as q^2 increases. An interesting example is the phenomenon of shadowing in electron-nucleus scattering, which has been observed³ in real photoproduction but has not yet⁴ been observed in electroproduction. Data were taken with heavy targets at selected kinematic points, attempting to detect shadowing effects at lower values of q^2 .

The production of resonances is a prominent feature of the photoproduction total cross section at low energy. Previous experiments have shown prominent bumps corresponding to production of resonances in inelastic electron scattering. At 4° counting rates are high, and by adopting experimental techniques designed to minimize systematic

errors as the energy loss in the inelastic scattering varies, we can carefully study the already observed enhancements and look for heretofore unobserved structure in inelastic scattering.

This paper reports the results of the analysis of this experiment. In Sec. I we discuss the experimental apparatus; in Sec. II, the data-analysis procedures; in Sec. III, some kinematics and definitions; and in Sec. IV, the results of the experiment.

I. EXPERIMENTAL APPARATUS

This experiment was carried out at the Stanford Linear Accelerator Center. Preliminary results were reported⁵ at the Electron-Photon Symposium held at Cornell in August of 1971.

A. Beam

The primary electron beam from the accelerator was used at energies of 4.5, 7, 10, 13, 16, 18, and 20 GeV. A momentum slit in the SLAC beam switchyard transport system defined the beam's energy-spread to $\pm 0.1\%$ for almost all the running conditions. The absolute-momentum calibration of the transport system was known to $\sim 0.1\%$ as defined by a flip coil in a duplicate magnet excited in series with the beam-line bending magnets. The electron current was set to keep the rate of detected particles at an average of less than one per $1.6 \mu\text{sec}$ beam pulse and varied from 3×10^8 to $10^{11} e/\text{pulse}$. The beam current was integrated using two nonintercepting toroid charge monitors⁶ which were intercalibrated with a Faraday cup and determined to have an accuracy better than 1%. The size of the beam at the target was typically 4 mm horizontally and 2 mm vertically, and the position and steering were checked by periodically inserting ZnS screens into the beam. After passing through the target, the beam was dumped outside the well-shielded experimental building.

B. Targets

During the experiment, we used a liquid hydrogen target, liquid deuterium target, and heavy targets of Be, Al, Cu, and Au. They were all mounted on a movable assembly, which enabled remote selection of the appropriate target. Parameters for the various targets⁷ are given in Table I. The hydrogen and deuterium targets were vertical cylinders with 0.0076-cm aluminum walls. The aluminum "empty" target was also constructed in a cylinder with walls six times thicker than the liquid target walls in order to achieve approximately the same target thickness in radiation lengths.⁸ The total amount of radiator for the targets is listed in Table II for reference.

C. Detector

The scattered electrons were detected in the SLAC 20-GeV spectrometer,⁹ shown in Fig. 1, which was surveyed in place at a laboratory angle of 4.000° . An electron first passes through the magnet transport system of the spectrometer, which disperses momentum in the vertical plane, and disperses the projected horizontal scattering angle in the horizontal plane. The first-order optics are such that parallel rays from a horizontal line source are focused to a point. The detector arrangement in the hut of the spectrometer is shown in Fig. 2. The particle traverses a Čerenkov counter (\check{C}) filled with nitrogen gas at atmospheric pressure, a scintillation counter TR1, five multiwire proportional chambers¹⁰ (three to measure the vertical position and two for the horizontal), two more scintillation counters (TR2 and TR3), three multiplicity counters (MULT) which sample the shower produced in one radiation length of lead, and a total absorption lead-lucite shower counter (TA). The event trigger was a coincidence between TR3 and TA (with a low discriminator threshold) during the

1.6 μ sec beam pulse. Counter and chamber dimensions are shown in Table III.

The vertical aperture of the spectrometer was restricted by slits which were set so as to pass particles with ± 4.25 mrad in ϕ , the vertical projected scattering angle. Using the reconstructed tracks in the proportional chambers, we further restricted events to ± 3.5 mrad in θ , the horizontal projected scattering angle, and to $\pm 1.6\%$ in $\Delta p/p$, the momentum acceptance of the spectrometer. Typical distributions for these quantities are shown in Fig. 3. These cuts on θ and $\Delta p/p$ are well within the full spectrometer aperture.

D. Data acquisition

The data from each accelerator pulse were transmitted to an online SDS 9300 computer which sampled a fraction of the events and wrote all the events onto magnetic tape for subsequent off-line analysis on the SLAC IBM 360/91 computer. The online electronics were designed to handle up to 3 events/pulse, increasing our data acquisition rate appreciably and reducing corrections for lost events at high counting rates. Signals from each wire in the chambers were amplified and sent to the counting area on coaxial cables, where they were fed into CAMAC latches which could be sequentially gated up to three times before being read out. In addition, for up to 3 events in the pulse, we recorded the pulse heights in the Čerenkov counter, the three multiplicity counters, and the TA. On-line histograms of these quantities as well as track reconstruction in the chambers, enabled us to monitor the performance of the hardware. The other quantities which would be needed to evaluate the cross section, such as charge and spectrometer momentum, were also written onto tape by the SDS 9300. In the two cycles of running, a total of 217 tapes were re-

TABLE I. Target parameters. The length of the heavy-target foils is the average thickness based on the measured weight and area. The indicated error is an estimate of possible nonuniformity in the region where the beam went through.

Target	Density (10^{20} nucleons/cm ²)	Length (cm)	Z	N	A
H (liquid)	2921.5 \pm 0.94%	6.952 \pm 0.4%	1	0	1.007 97
D (liquid)	3605.8 \pm 1.26%	7.117 \pm 0.4%	1	1	2.014 71
Al ("empty")	55.1 \pm 2%	0.0914	13	14	26.98
Be	418.1 \pm 2%	0.344	4	5	9.012
Cu	11.88 \pm 3%	0.0145	29	34.62	63.54
Au	1.241 \pm 10%	0.0021	79	118	197

TABLE II. Target radiation lengths. The quantity t_b is the thickness in radiation lengths of all material upstream of the target plus $\frac{1}{2}$ of the thickness of the target. The quantity t_a is the thickness of all material between the target and the spectrometer vacuum, including $\frac{1}{2}$ of the target thickness.

	t_b (10^{-3} radiation lengths)	t_a (10^{-3} radiation lengths)
H (liquid)	5.459	11.129
D (liquid)	6.348	12.018
Be	5.64	11.451
Al	5.30	11.111
Cu	5.382	11.193
Au	3.682	9.493

corded. These were condensed off-line, yielding 108 tapes to be analyzed.

II. DATA ANALYSIS

The data taking was divided into two modes of running: discrete mode and scan mode. These were processed in a similar manner off-line.

A. Discrete mode

In this type of operation, the parameters for the run were entered and data were taken at a single momentum setting. This procedure was followed for most of the structureless part of the data. In this region the spectrometer momentum was changed between runs by amounts much larger

than the spectrometer's momentum bite. For each setting, the on-line computer set the currents in the magnets and recorded the quantities needed to calculate the cross section: scalars, charge monitors, magnet parameters, etc.

B. Scan mode

In order to minimize the effect of nonuniform bin efficiencies that might exist in the wire chambers and which might cause erroneous bumps in the missing-mass spectrum, we ran the spectrometer in the scan mode.¹¹ The computer automatically changed the spectrometer momentum setting by a small fraction of the momentum bite after a predetermined number of incident electrons had

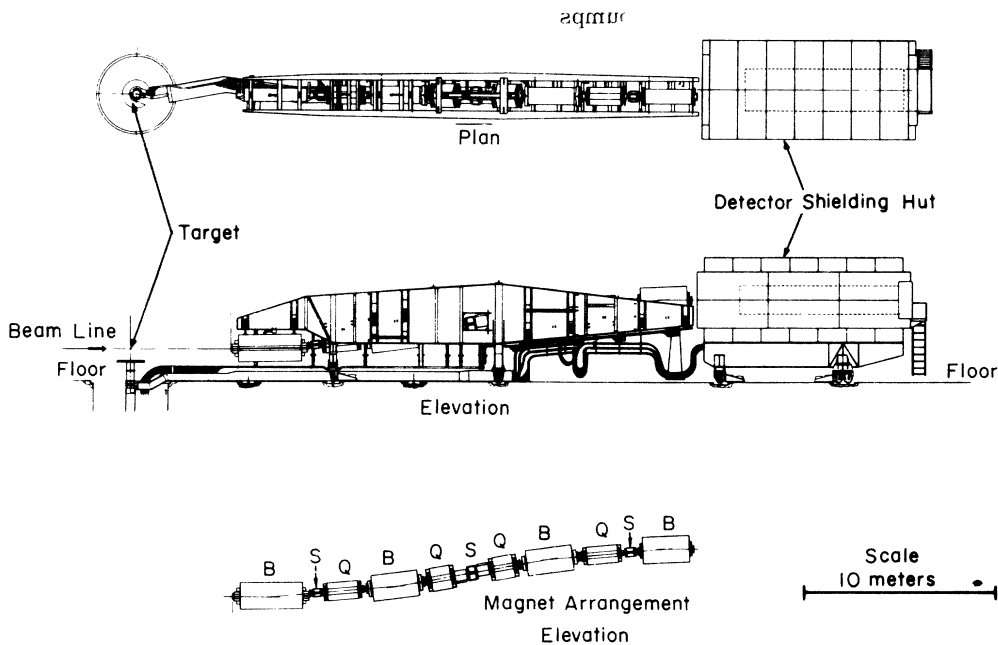


FIG. 1. Plan and elevation views of the SLAC 20-GeV spectrometer. The arrangement of magnets is shown at the bottom of the picture where B=bending magnet, Q=quadrupole, S=sextupole.

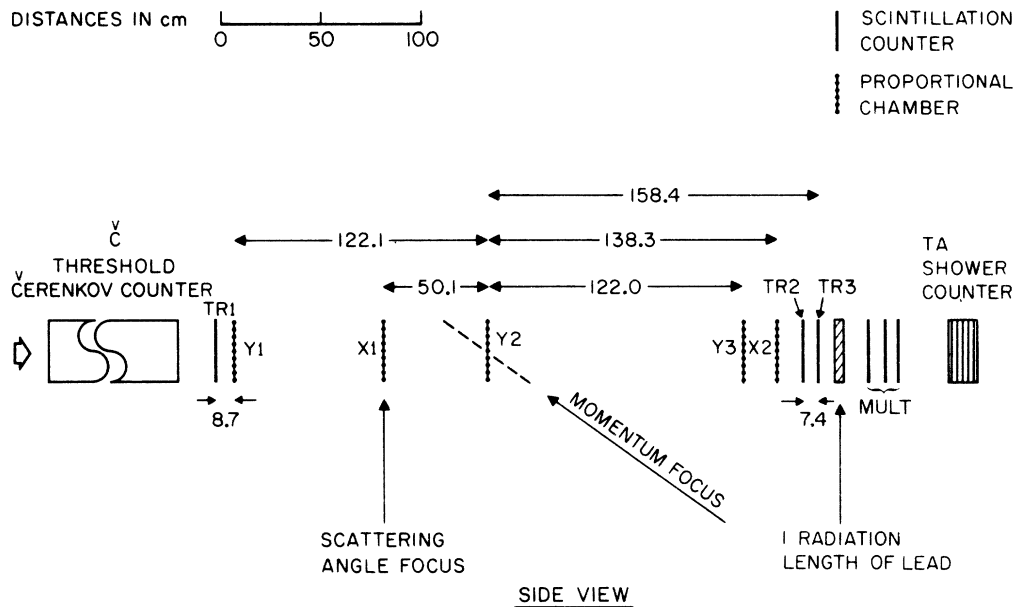


FIG. 2. The detector arrangement in the hut of the 20-GeV spectrometer.

been obtained. Each momentum setting, called a "minirun," was analyzed off-line as a separate run. By using this technique, each missing-mass bin receives data averaged over all the wires, which also minimizes errors caused by any variation in the detector's solid angle. Since we were interested in looking for small or narrow bumps in the cross section, removing erroneous sources that might cause such effects was important. Typically, the momentum change per minirun corresponded to one wire spacing or 0.07% in $\Delta p/p$, which is approximately the momentum resolution of the spectrometer. For most scans, the number of events measured gave $\pm 2\%$ statisti-

cal error in bins that were $\approx 0.1\%$ of the incident energy.

C. Data reduction

For each run, various cuts were applied to the data to select only events in which the detected particle was an electron. From all the runs, distributions of pulse height for the TA, MULT, and \check{C} counters were made. For the TA, the mean and standard deviation of the distribution were determined as a function of scattered energy, E' , and a cut placed for all the data at 3.5 standard deviations below the mean. This has an ef-

TABLE III. Counter and chamber dimensions (in cm).

	Horizontal	Vertical	Thickness	No. of wires
TR1	14.8	13.5	0.32	
TR2	11.2	11.2	0.64	
TR3	15.2	16.9	1.27	
TA	29.2	36.8	(16 radiation lengths)	
MULT 1, 2, 3	20	20	0.64	
\check{C}	20	20	285 N ₂ at 1 atm. 0.0685 Al 0.0127 Mylar	
Chamber 1 (Y)	18.8	14.0		70
Chamber 2 (X)	16.4	18.8		82
Chamber 3 (Y)	18.8	15.6		78
Chamber 4 (Y)	18.8	18.0		90
Chamber 5 (X)	16.0	18.8		80

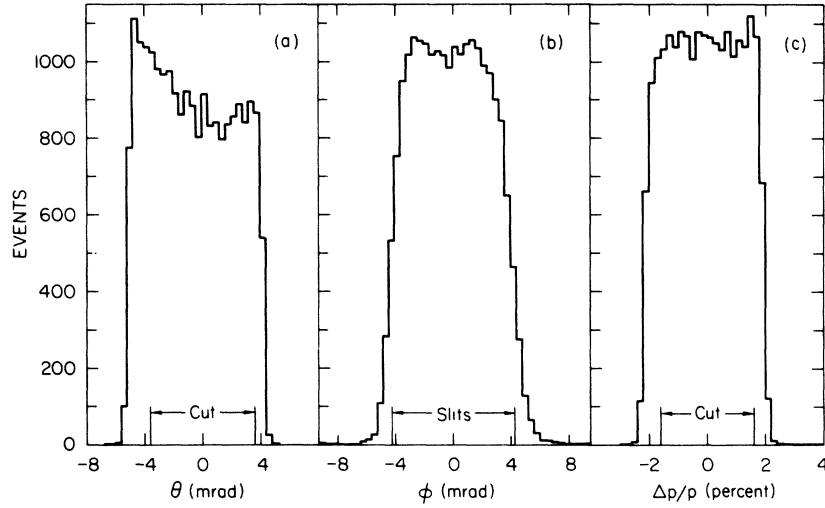


FIG. 3. Distributions in the reconstructed scattering coordinates of all events satisfying the trigger at incident energy 13 GeV and spectrometer momentum 9.13 GeV/c: (a) The horizontal projected scattering angle θ . The shape of the distribution reflects the $1/\sin^4(\frac{1}{2}\theta)$ of the cross section; the cut at ± 3.5 mrad is shown. (b) The vertical projected scattering angle ϕ . The position of the vertical slits at ± 4.25 mrad is shown. (c) The fractional momentum $\Delta p/p$. The cut at $\pm 1.6\%$ is shown.

efficiency of 0.9998, assuming a Gaussian distribution for the low-energy side of the data. Other reasonable assumptions about the spectrum shape that are consistent with the data also yield an efficiency of ≈ 1.0 with no appreciable systematic error. Sample TA distributions are shown in Fig. 4(a) for typical running conditions and in 4(b) for one of the worst conditions.

The \check{C} counter was able to distinguish electrons from π 's when the momentum was less than 6 GeV/c. For all data below this energy, a cut was applied to the \check{C} pulse height that was 0.98 efficient for electrons. This efficiency was determined from runs where the TA cut alone was sufficient to eliminate almost all the π 's. Figure 4(b) also shows the TA distribution with the \check{C} cut applied to eliminate the pion background.

For ten runs with the momentum between 6 and 10 GeV/c, the TA counter alone was inadequate to eliminate the pion background. For these runs, the multiplicity-counter pulse-height information was used to eliminate the remaining π 's. The efficiency of this cut depended on energy and was determined by looking at runs for which the TA and \check{C} counters were adequate. Figure 5 shows the measured efficiency which varied from 0.945 at 6 GeV/c to 0.96 at 10 GeV/c.

Corrections were applied to the data for the \check{C}

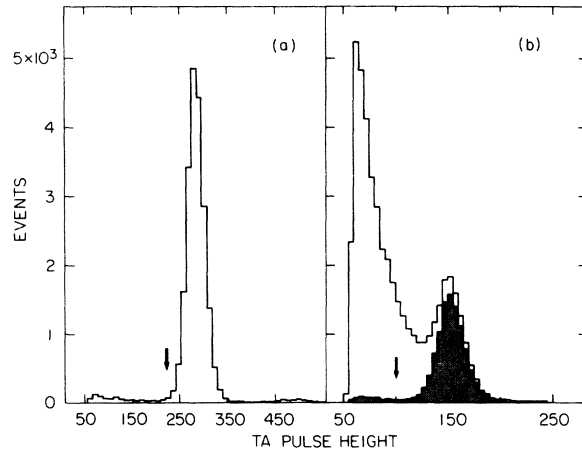


FIG. 4. Event distribution in the pulse height from the TA counter. The arrow indicates the position of the TA pulse-height cut. The lack of events below channel 50 is due to the discriminator threshold setting. Zero pulse height should typically appear near channel 40. (a) Typical running conditions, $E_0 = 13$ GeV, $E' = 9.13$ GeV. The peak shows the clean electron signal; a very small two-electron peak can be seen around channel 475. (b) One of the worst conditions, $E_0 = 20$ GeV, $E' = 4.14$ GeV. The shaded region shows the data after a cut on the pulse height from the Cerenkov counter is made.

and MULT efficiencies. There were also electronics dead-time counting-rate corrections which were $<0.5\%$. During the data taking, circuits were incorporated to measure this dead time and corrections were applied for it. In addition we made corrections for events lost due to computer dead time by comparing the number of events recorded on tape to the number seen by a fast hardware scaler. This varied from run to run and was about 0.5% on the average. There was also a correction for the efficiency of the proportional wire chambers, which was about 95% averaged over the experiment.

The events were processed off-line and a summary of each run and minirun, including counter efficiencies, run parameters, and cross sections, was written onto disk. There were approximately 10 000 runs and miniruns recorded.

The data were divided into larger blocks, called lines, defined as containing all the runs (or miniruns) with the same target and incident energy. These lines constitute the raw data spectra. A typical line is shown in Fig. 6.

The counts recorded in the hydrogen and deuterium running include target-wall events which were subtracted using data from the dummy target. For all targets, some events arise from charge-symmetric processes such as π^0 production, with subsequent conversion of the photon into e^+e^- pairs. In order to obtain the cross section for only the scattered e^- events, measurements were

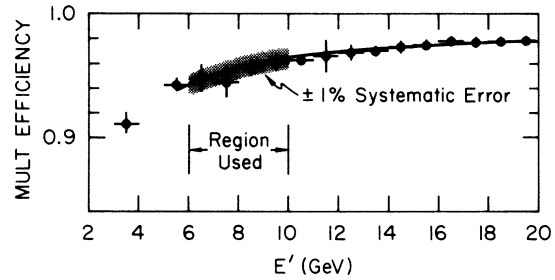


FIG. 5. Measured efficiency of the MULT pulse-height cut as a function of detected particle energy. The curve is the function used to correct the data in the region shown. The data points show the mean and standard deviation of all measurements from runs in each bin of E' .

taken with the spectrometer set to detect e^+ and the cross section from these runs was subtracted from the corresponding e^- run. This affects only the very low-energy ends of the lines. Figure 7 shows the worst case of such a subtraction on hydrogen. After these corrections were made, the data were ready for radiative corrections.

D. Radiative corrections for hydrogen

1. Elastic tail

One of the processes contributing to the inelastic yield is the radiative tail from elastic scattering.

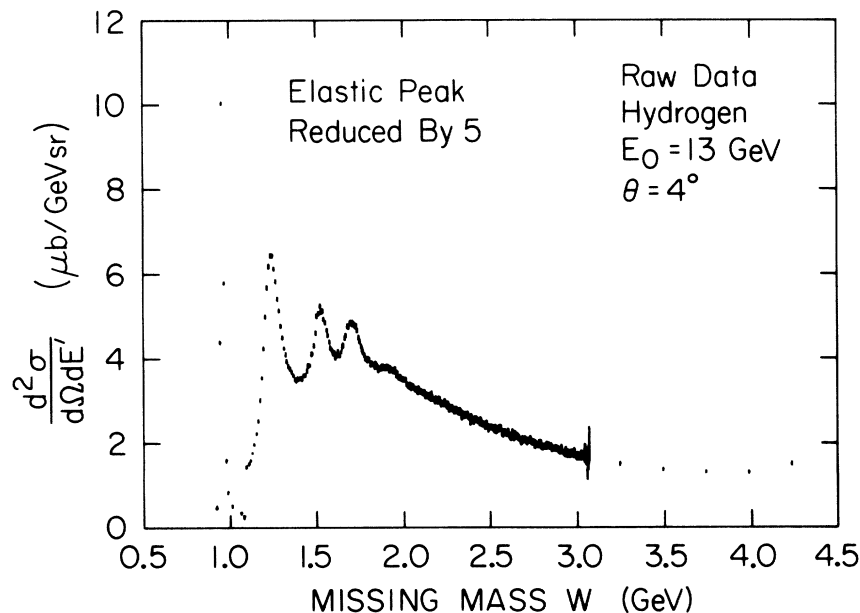


FIG. 6. The raw scattering cross section $d^2\sigma/d\Omega dE'$ for hydrogen at $E_0=13$ GeV. No dummy subtractions, positron subtraction, or radiative corrections have been made. The elastic peak is reduced by 5.

We calculated the elastic tail cross section following the procedure given in the thesis of Miller.¹² Details of the calculations are given in Appendix A. The energy of the incident beam was used as an adjustable parameter in this calculation to match the theoretical tail with the data between the elastic peak and one-pion threshold. There was one adjustment for each line of data taken. In all cases the amount of change to the incident energy was less than 0.1%, which is smaller than the estimated error due to the energy-defining slits in the accelerator. An example of the agreement between theory and experiment is shown in Fig. 8. This calculated elastic tail cross section was then subtracted from each point on the line and the resulting cross sections were recorded to be used as input for the remaining radiative corrections. The errors were propagated as though there were no error on the calculated tail. The subtraction was as much as 50% for the lowest E' point on each line. We estimate the systematic error in the calculated tail as $\pm 5\%$, which contributes an error of 5% to the subtracted cross sections for the worst case. For most of the data the error in the subtracted cross section is much smaller than this figure.

2. Inelastic corrections

To calculate the inelastic radiative corrections for a measured cross section at incident energy

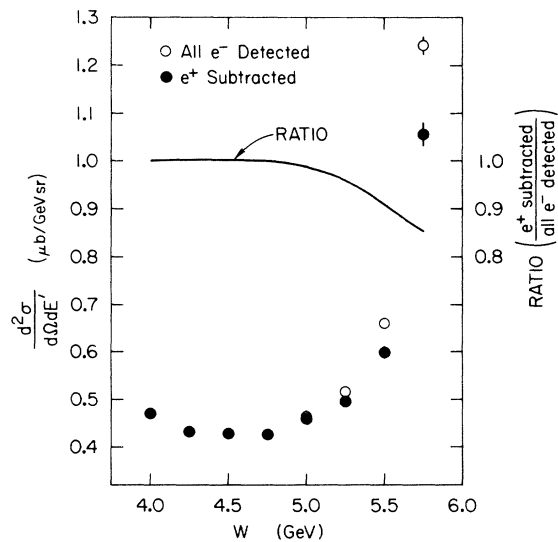


FIG. 7. Positron subtraction for the worst line, $E_0 = 20$ GeV and the hydrogen target. The open circles are the cross sections from all detected electrons; the closed circles are the cross sections after the positron cross sections are subtracted. The solid line is the ratio of the cross sections before and after subtractions.

E_0 and scattered energy E' , a knowledge of the cross sections for all lower values of E_0 and for all higher values of E' is required. Since only some of these are measured experimentally, the usual procedure¹³ has been to use the measured points and interpolate in order to determine the cross section for any desired value of (E_0, E') . Numerous interpolations make it difficult to assign errors to the final values of cross sections, as this procedure tends to mix systematic and statistical errors and to correlate the errors among the data points. Further, using the peaking approximation (see Appendix A), the separation of the two-dimensional integral into two one-dimensional integrals plus one single function makes the errors depend somewhat upon the choice of an arbitrary parameter, ΔE , used to split the integration region.

In this paper we have adopted a new approach to the radiative corrections which is briefly described here. Cross sections obtained by applying the radiative corrections procedure of Mo and Tsai¹³ are represented by an approximate expression containing 30 parameters. Using this fit and the formulas of Ref. 13 and Appendix A, we calculated a ratio of cross sections with and without radiative corrections. Each measured cross section was then corrected by this ratio. The statistical errors are obtained by multiplying the uncorrected data errors by the same ratio. The newly corrected data were then refitted and the process iterated to obtain the final answers. The use of a smooth model eliminates the spurious amplifications of point-to-point statistical fluctuations in the data. We estimate a possible systematic uncertainty in the corrected data varying

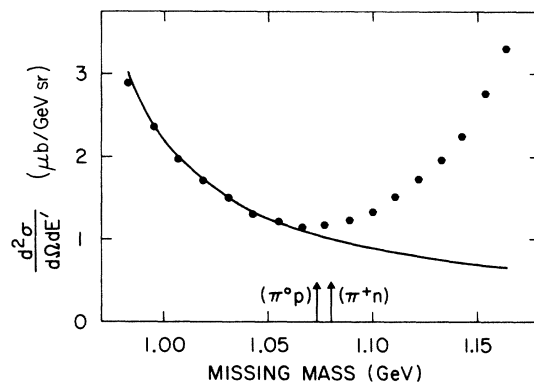


FIG. 8. Experimental value of the cross section $d^2\sigma/d\Omega dE'$ vs missing mass for the 13-GeV hydrogen data. The line is the calculated elastic-tail contribution. The errors on the data points are smaller than the symbols.

from $\pm 3\%$ near inelastic threshold to $\pm 5\%$ at the low- E' end of the lines. A major contribution to this estimate arises from uncertainties in the calculations of the multiple photon emission.

E. Radiative corrections for deuterium and higher- Z targets

Three radiative processes contributing to the observed cross section for heavy targets are the radiative tail from elastic nucleus scattering, tails from quasielastic electron-nucleon scattering, and processes in the inelastic continuum.

1. Elastic tail

The elastic form factor is a rapid function of q^2 , so this process affects mainly the very-low- E' region of each line where hard photons can be radiated, yielding an effective q^2 [$\approx 4E'^2 \sin^2(\frac{1}{2}\theta)$, for small angles] that is small. The formulas used for the elastic radiative tail are the same as those for hydrogen, with the structure functions replaced by their counterpart for each target (see Appendix A). We caution that the one-photon-exchange approximation has been used and the corrected cross section for the high- Z elements is suspect where the calculated elastic tails are large.

2. Quasielastic tail

For most of the data, a larger contribution to the observed cross section is that from the quasi-elastic tail. This tail arises from elastic scattering from individual nucleons in the nucleus. To account for the bound nature of the nucleons we have used the technique suggested by Atwood and West.¹⁴ The exact formulas will be found in Appendix A. An example of this calculation is shown in Fig. 9, which shows the observed scattering cross section for the deuterium data at 4.5 GeV and the calculated quasielastic and elastic peaks with radiative effects and resolution included.

One modification must be made to the impulse approximation calculation when the quasielastic cross section is calculated for the low- q^2 data. As is known from low-energy electron-deuteron scattering,¹⁵ the inelastic cross sections are suppressed from their simple incoherent sum due to the probability of coherent, i.e., elastic, scattering. This introduces a factor $[1 - F_{el}^2(q^2)]$ into the quasielastic electric form factor, where $F_{el}(q^2)$ is the nuclear elastic form factor. For the lowest-energy line at q^2 of 0.1 (GeV/c)^2 , this is a 15% correction to the quasielastic peak on deuterium.

These elastic and quasielastic tails were calculated as described in Appendix A and subtracted

from the data. The inelastic radiative correction for deuterium was performed as for hydrogen. No inelastic radiative corrections were made on the nuclei heavier than deuterium.

For all the hydrogen and deuterium data, the final cross sections are shown in Fig. 10 for values of W up to 3 GeV and a complete table has been deposited with the National Auxiliary Publication Service (NAPS).^{15a} Figure 11 displays the q^2 - ν kinematic plane and shows the region covered by this experiment.

F. Errors

The cross-section errors are statistical only except for the ten values of E' at which the multiplicity counters were used for electron identification. For these runs, we have included a measure of their relative systematic error by adding 1% linearly to the statistical error.

For almost all the data, the systematic errors are greater than the statistical errors. We consider the following sources of systematic error:

(1) *Number of target nuclei.* For each run and minirun and approximately every minute in the long runs, we recorded the liquid target temperatures using four hydrogen vapor-pressure thermometers. Measurements were taken both above

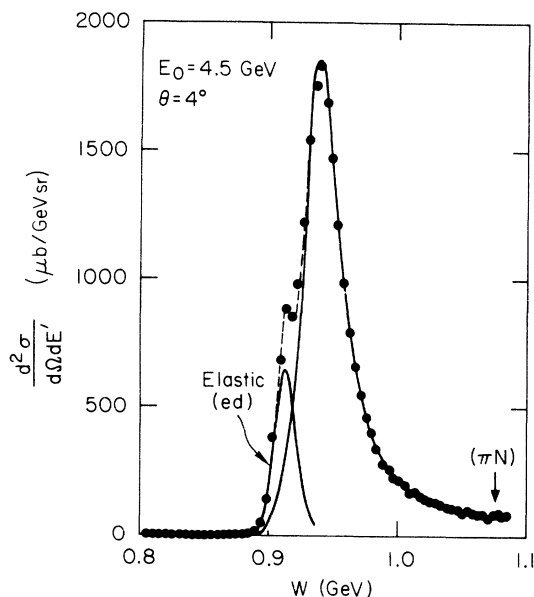


FIG. 9. Experimental values of the cross section $d^2\sigma/d\Omega dE'$ vs missing mass for the 4.5-GeV deuterium data. The lines are the calculated elastic and quasielastic peaks and radiative tails with effects of momentum resolution included. The statistical errors on the data points are smaller than the symbols.

and below the target volume on both hydrogen and deuterium. The results for the four values of pressure are shown as the first line in Table IV. The largest contributions to the errors in these pressures are from the absolute calibration of the digital voltmeter and reference voltage source. This pressure is then converted to temperature¹⁶ with negligible additional error (<0.1%). The density is calculated for each of the four values of temperature,¹⁷ which adds an error of $\pm 0.1\%$ for hydrogen and $\pm 0.6\%$ for deuterium to the propagated error from the vapor pressures. A systematic error was assigned to the target density, based on the over-all spread of the observed temperature distributions. Combining these re-

sults with the measurement of the target lengths and its error yields a systematic uncertainty in the average target density of $\pm 0.94\%$ for hydrogen and $\pm 1.26\%$ for deuterium.

(2) *Number of electrons.* The estimated systematic error in the toroid charge monitor is $\pm 1\%$. Both the toroids were calibrated using pulsers to simulate the beam by discharging capacitors through single turns on the toroid cores.⁶ The stability of these calibrations was checked frequently during the data taking. In addition the toroids were compared against a Faraday cup. Consideration of the results of these various calibrations plus estimates of the expected levels of absolute accuracy leads us to assign $\pm 1\%$ as

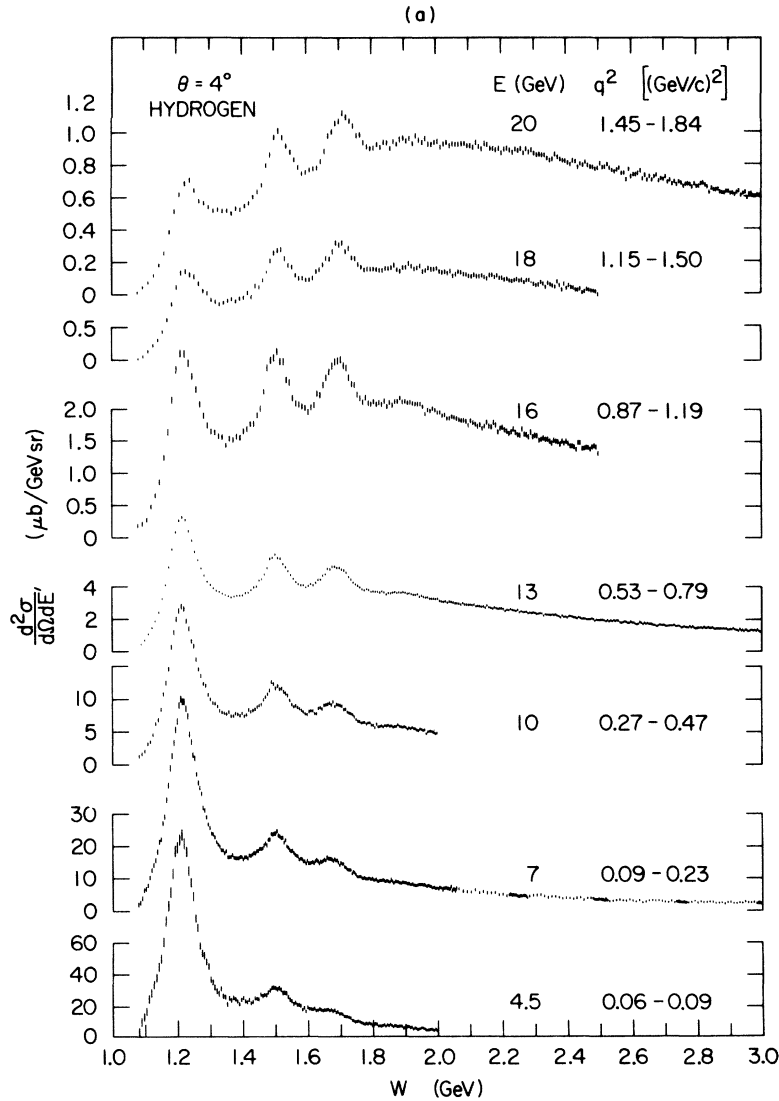


FIG. 10. (Continued on following page)

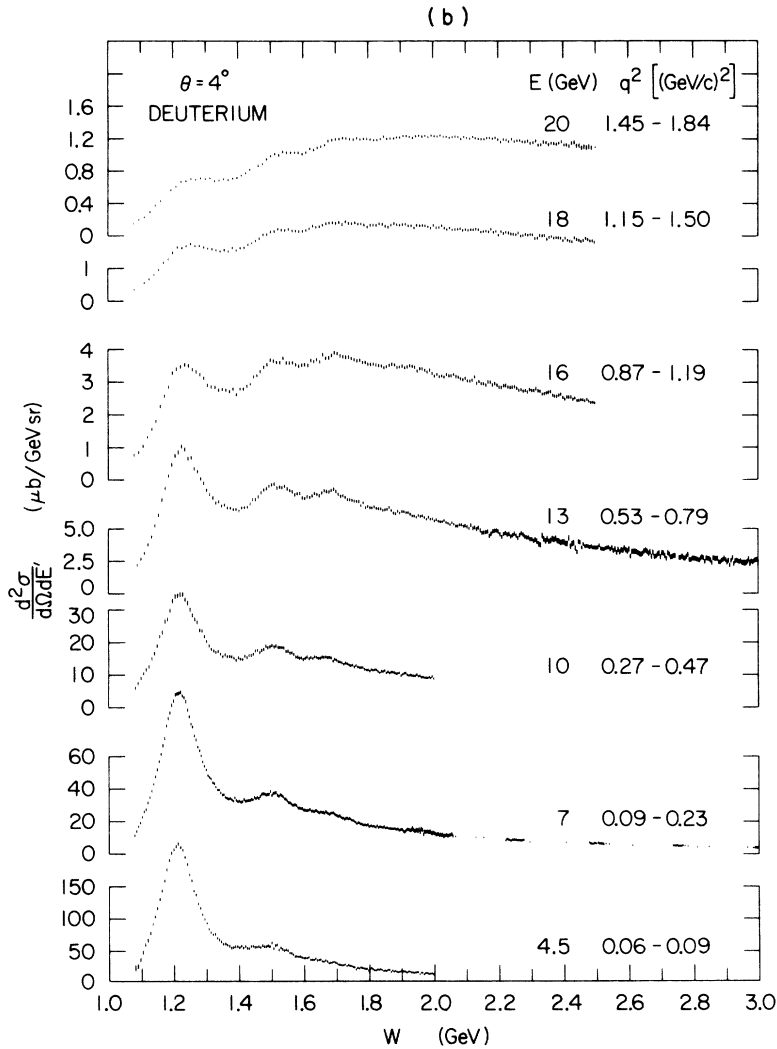


FIG. 10. Experimental values of the cross section $d^2\sigma/d\Omega dE'$ vs missing mass for all the data. The incident energy and q^2 range (q^2 increasing with decreasing W) for each line are shown. (a) Hydrogen. (b) Deuterium.

the estimated systematic error in the incident beam charge.

(3) *Solid angle.* Optics measurements made on the 20-GeV spectrometer yield an estimate of the systematic error of $\pm 2\%$ for the solid angle. We reanalyzed the optics measurements, taking account of the restricted aperture and small effective transverse target size appropriate to this experiment. In addition, for this experiment, we made checks on the optics coefficients used in reconstructing events by changing the cuts on ϕ (the vertical projected scattering angle), θ (the horizontal projected scattering angle), and $\Delta p/p$.

The cross section shows no variation outside of statistical errors. We also looked at the cross sections for a given E' as the spectrometer momentum was changed during the scanning procedure; the distributions are also consistent with statistical errors. Based on these studies, we estimate $\pm 2\%$ as the systematic error in solid angle.

(4) *Track-reconstruction efficiency.* Each event with a signal from TR1 should have a reconstructed track hitting both TR1 and TR3. The track-reconstruction efficiency was calculated, run by run (minirun by minirun), by comparing

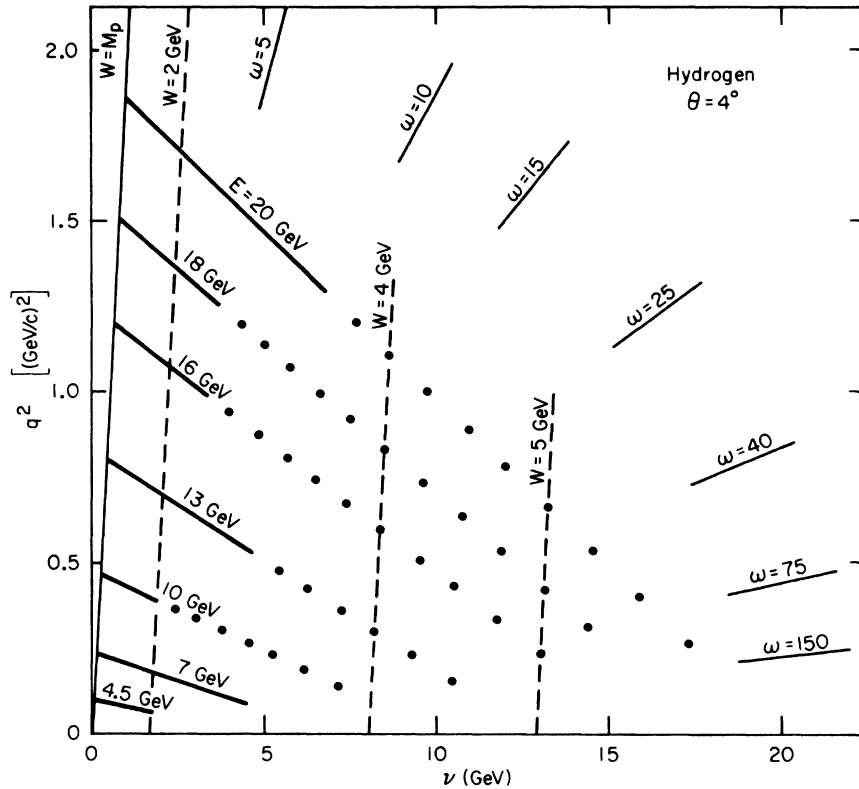


FIG. 11. Kinematic (q^2, ν) plane showing the location of the measured 4° cross sections. The heavy lines represent "scanned" data, where the measurements from each run overlapped. Lines of constant missing mass W are shown dashed, and lines of constant $\omega = 2M\nu/q^2$ are indicated.

the number of events with reconstructed tracks hitting the counters TR1 and TR3 (taking into account the measurement resolution) to the number of events with a signal from TR1. The average for all runs was 95%. This includes the intrinsic wire-chamber inefficiency and effects of multiple tracks. The FWHM (full width at half maximum) of the distribution of the efficiencies is 2%, and we estimate the systematic error as $\pm 1\%$ from this source.

In Table V we summarize these sources of systematic error. Combining in quadrature yields an over-all uncertainty of $\pm 2.62\%$ in hydrogen and $\pm 2.75\%$ for deuterium. In ratios of deuterium to hydrogen, the over-all uncertainty is estimated to be only $\pm 1.57\%$, since some of the above-mentioned errors cancel.

Systematic errors also arise from the corrections made for radiative processes. For the hydrogen cross sections errors arise in subtracting

TABLE IV. Hydrogen and deuterium density. Measured values of the vapor pressure below and above the target volume and the calculated average density which is the mean of the extreme values of the two measurements for each target. The errors are estimates of the systematic uncertainty arising from the measurements and the known temperature-density relationship.

	Hydrogen		Deuterium	
	Lower	Upper	Lower	Upper
Vapor pressure (atm.)	1.0897 $\pm 4.9\%$	1.1480 $\pm 5.2\%$	1.0970 $\pm 5.2\%$	1.1029 $\pm 5.3\%$
Temperature ($^\circ\text{K}$)	20.560 $\pm 0.83\%$	20.741 $\pm 0.88\%$	20.582 $\pm 0.88\%$	20.601 $\pm 0.89\%$
Density (g mole/cm ³)	0.03495 $\pm 0.38\%$	0.03484 $\pm 0.40\%$	0.04218 $\pm 0.84\%$	0.04217 $\pm 0.85\%$
Av. density (g mole/cm ³)	0.03489 $\pm 0.54\%$		0.04218 $\pm 0.86\%$	

the elastic scattering tail and in the inelastic continuum corrections. The error on the elastic tail is estimated to be $\pm 5\%$; this results in an error of $\lesssim \pm 1\%$ for $E' \geq 5$ GeV growing to $\pm 5\%$ at our lowest value of $E' = 2.6$ GeV. Over most of the range of the hydrogen data the error in the cross section from the inelastic radiative corrections is $\pm 3\%$. The error from this source is estimated to increase to $\pm 5\%$ for $W \geq 5$ GeV.

For deuterium cross sections three radiative processes contribute (see Sec. II E), but only two of these processes contribute significant errors to the final cross sections, since the elastic scattering falls off rapidly even for small values of q^2 . The calculation of the quasielastic scattering tails depends on knowledge of both the proton and neutron form factors. The latter are not known as well as those for the proton, so the error on the quasielastic tail is estimated to be $\pm 7.5\%$, somewhat larger than for the hydrogen case. This error in the tail results in an error in the final deuterium cross sections of $\lesssim \pm 1.5\%$ for $E' \geq 5$ GeV growing to $\pm 7.5\%$ at $E' = 2.6$ GeV. The error arising from inelastic corrections is assumed to be the same as in the case of hydrogen.

In the ratio of D/H, errors from radiative corrections tend to cancel, but the uncertainty in the neutron form factors generates some uncertainty in the relative values of the quasielastic tail in deuterium when compared with the elastic tail in hydrogen. We estimate that an error of $\pm 5\%$ might persist in the deuteron quasielastic tail calculation. For our final n/p ratio this leads to an estimated error due to radiative corrections of $\lesssim \pm 1\%$ for $E' \geq 5$ GeV, growing to $\pm 5\%$ at $E' = 2.6$ GeV.

The above estimates of systematic error due to radiative corrections should be combined with the

TABLE V. Sources of systematic uncertainties in the absolute cross sections. Estimates of the systematic errors contributing to the absolute cross-section measurements. Errors due to the following sources were smaller and were neglected: rate effects, incomplete π - e separation, errors in the E_0 and θ measurements, purity of the gases used to fill the liquid targets. In addition to these systematic errors there are also errors due to radiative corrections which are discussed in the text.

	Hydrogen	Deuterium
No. of target nuclei	$\pm 0.94\%$	$\pm 1.26\%$
No. of incident electrons		$\pm 1\%$
Solid angle		$\pm 2\%$
Reconstruction efficiency		$\pm 1\%$
Total	$\pm 2.62\%$	$\pm 2.75\%$

other sources of systematic errors enumerated in Table V.

G. Deuterium analysis

1. Extraction of neutron information

The scattering from deuterium is approximately the sum of scattering from the proton and the neutron. Our purpose in measuring deuterium cross sections was to learn about the neutron, so the contribution from the proton must be accounted for. We have used the same formalism (Atwood and West)¹⁴ as for the quasielastic scattering to calculate the cross section for the proton in the deuteron, the "smeared" cross section.

We first fitted all the hydrogen data to the same function as used in the radiative correction procedure. This model, σ_H^M , is used to perform the smearing integral¹⁴ and gives us σ_H^{MS} , the smeared model, from which we calculate the smearing ratio σ_H^M/σ_H^{MS} . In Fig. 12 we plot these ratios as a function of W for the different lines of data. Since we will restrict the analysis to values of $W > 2$ GeV, this correction is small, $\lesssim 2\%$. Using the smearing ratio we calculate a smeared proton cross section as $\sigma_p^S = \sigma_H/(\sigma_H^M/\sigma_H^{MS})$, where σ_H is the experimentally measured hydrogen cross section. Subtraction yields the smeared neutron cross section:

$$\sigma_n^S = \sigma_D - \sigma_p^S. \quad (1)$$

Since the smearing correction is small, we assign no additional systematic error to the neutron data and just consider the deuterium and hydrogen errors.

2. Glauber correction

Based upon the strength of the electromagnetic interaction, the mean free path of a photon in

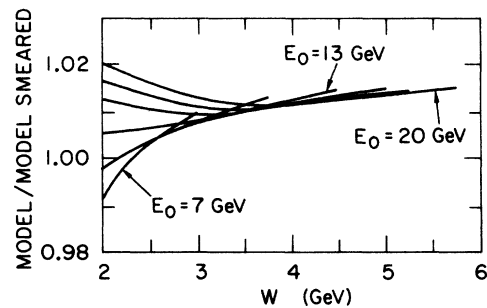


FIG. 12. The smearing correction applied to the hydrogen measurements when analyzing deuterium. The different lines are the six incident energies with data above $W = 2$ GeV.

nuclear matter is quite large. However, theories like vector-meson dominance have predicted¹⁸ that shadowing in electron scattering should occur and that a correction for this effect would have to be made. Since experimental measurements of the scattering on heavy nuclei by electrons show no significant shadowing (see Ref. 4 and Sec. IV F) we have made no Glauber corrections to our deuterium data.

III. KINEMATICS AND DEFINITIONS

Let us consider the process shown in Fig. 13. An electron of energy E_0 in the laboratory is incident upon a nucleon of mass M . We assume that one-photon exchange is adequate for describing this process. The momentum (energy) E' and angle θ of the scattered electron are measured, completely defining the virtual photon. We then define

$$\begin{aligned} q^2 &= 4E_0E' \sin^2(\tfrac{1}{2}\theta), \\ \nu &= E_0 - E', \\ W^2 &= M^2 + 2M\nu - q^2. \end{aligned} \quad (2)$$

W is the missing mass, or effective mass, of the unobserved particles produced in the reaction. In terms of these, two common scaling variables¹⁹ are

$$\begin{aligned} \omega &= 1/x \\ &= 2M\nu/q^2, \\ \omega' &= 1/x' \\ &= (2M\nu + M^2)/q^2 \\ &= 1 + W^2/q^2. \end{aligned} \quad (3)$$

The cross section can be written as

$$\begin{aligned} \frac{d^2\sigma}{d\Omega dE'} &= \frac{\alpha^2 \cos^2(\tfrac{1}{2}\theta)}{4E_0^2 \sin^4(\tfrac{1}{2}\theta)} \\ &\times [W_2(q^2, \nu) + 2 \tan^2(\tfrac{1}{2}\theta)W_1(q^2, \nu)], \end{aligned} \quad (4)$$

where α is the fine-structure constant $\alpha \approx 1/137.036$.

The structure functions W_1 and W_2 are functions of the Lorentz invariants, q^2 and ν . This form for the cross section is valid for one-photon exchange and for an unpolarized beam and target²⁰ assuming conservation of parity, and Lorentz and gauge invariance. Because the photon is virtual, it can have both longitudinal and transverse polarizations. The value of the polarization parameter, ϵ , is defined as follows:

$$\epsilon = [1 + 2 \tan^2(\tfrac{1}{2}\theta)(1 + \nu^2/q^2)]^{-1}. \quad (5)$$

In analogy with photoproduction, we can also write the cross section in the form²¹

$$\frac{d^2\sigma}{d\Omega dE'} = \Gamma_T(\sigma_T + \epsilon\sigma_L), \quad (6)$$

where the "flux" of virtual photons is given by

$$\begin{aligned} \Gamma_T &= \frac{\alpha}{2\pi^2} \frac{K}{q^2} \frac{E'}{E_0} \frac{1}{1 - \epsilon}, \\ K &= \frac{W^2 - M^2}{2M}. \end{aligned} \quad (7)$$

K is the photon energy needed to produce the mass W in photoproduction. The transverse and longitudinal cross sections, σ_T and σ_L , are related to W_1 and W_2 by

$$\begin{aligned} W_1 &= \frac{K}{4\pi^2 \alpha} \sigma_T, \\ W_2 &= \frac{K}{4\pi^2 \alpha} \frac{q^2}{q^2 + \nu^2} (\sigma_T + \sigma_L) \end{aligned} \quad (8)$$

and have the limiting property,

$$\lim_{q^2 \rightarrow 0} \sigma_T(q^2, \nu) = \sigma_{\gamma p}(K), \quad \lim_{q^2 \rightarrow 0} \sigma_L(q^2, \nu) = 0. \quad (9)$$

We define the variable $R = \sigma_L/\sigma_T$, and write the relation between W_1 and W_2 as

$$\frac{W_2}{W_1} = \frac{1 + R}{1 + \nu^2/q^2}. \quad (10)$$

The relative contribution to the measured cross section of W_1 and W_2 is then given by

$$\begin{aligned} \frac{2W_1 \tan^2(\tfrac{1}{2}\theta)}{W_2} &= \frac{2 \tan^2(\tfrac{1}{2}\theta)(1 + \nu^2/q^2)}{1 + R} \\ &= \frac{1 - \epsilon}{\epsilon(1 + R)}. \end{aligned} \quad (11)$$

For most of the kinematic range covered by this experiment, the W_1 contribution to the cross section is considerably smaller than that of W_2 .

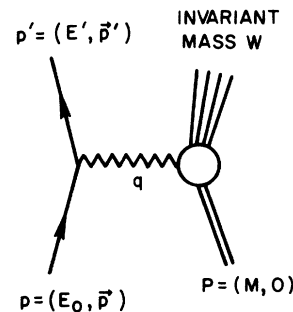


FIG. 13. Feynman diagram for electron-proton scattering in the one-photon approximation.

IV. RESULTS

A. Elastic electron-proton scattering

The elastic-scattering cross section was determined for each of the seven incident energies. An example of the data at one of the energies is shown in Fig. 14. We have plotted the measured cross section, $d^2\sigma/d\Omega dE'$ versus the "missing energy," calculated as follows. For each event, the energy of an elastically scattered electron is calculated corresponding to the measured scattering angle. Then, the measured energy is subtracted from this quantity. Thus, elastic scattering corresponds to missing energy of zero. The width of the raw data peak is due to instrumental resolution and radiative processes. Using the formulas from Ref. 12, we have corrected the data for soft-photon radiation. This unfolded spectrum is also shown in the figure. The remaining

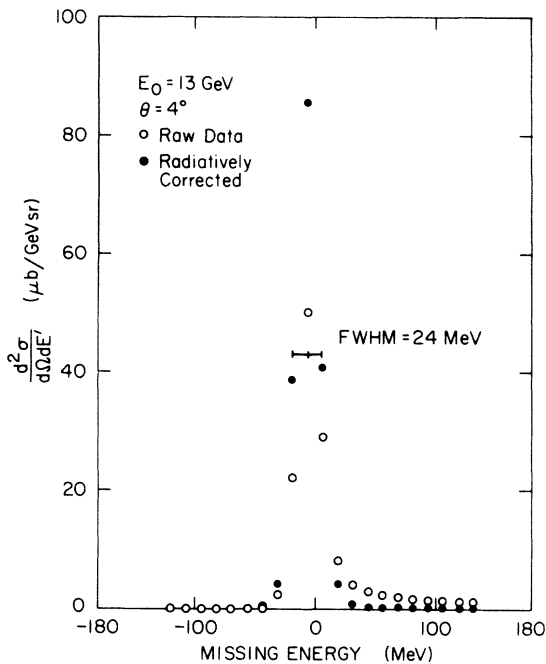


FIG. 14. Experimental values of the cross section $d^2\sigma/d\Omega dE'$ for elastic electron-proton scattering at $E_0=13$ GeV. The open circles are the data before radiative corrections; the closed circles are the data after unfolding the spectrum to take radiative effects into account. The energy resolution at this energy is 24 MeV FWHM arising from the incident-beam-energy definition. The errors are smaller than the symbols. The data are plotted vs missing energy, the difference between the electron energy corresponding to elastic scattering and the measured energy of the detected electron. The slight offset from zero is an example of the differences in calibration of the spectrometer momentum and incident beam energy.

width is due to resolution and has as its main contribution the FWHM of the incident beam, which corresponds to 24 MeV in missing energy in this example. The instrumental resolutions in the spectrometer of $\pm 0.07\%$ in $\Delta p/p$ and ± 0.05 mrad in θ are negligible when added in quadrature. We determined the total cross section by integrating over the scattered electron's energy. The results for $d\sigma/d\Omega$ for each of the energies are listed in Table VI, along with the corresponding values of q^2 and the errors of each measurement.

In order to compare these measurements with other experiments, we have calculated the expected 4° cross sections using data²² in the range of q^2 from 0 to 2 $(\text{GeV}/c)^2$ for which more than one angle has been measured at each q^2 . In Fig. 15, we plot as a function of $(q^2)^{1/2}$ our data and the extrapolated data from other experiments, both divided by the cross section calculated using the dipole approximation, form-factor scaling, and the Rosenbluth²³ approximation. We conclude that our data agree with the other available measurements within our systematic errors.

B. Neutron-proton comparison

Previous results²⁴ have shown that the deuteron exhibits scaling behavior similar to that of the proton. The neutron structure function is quite different from that of the proton at large x' . Previously published electroproduction data have not covered the very-low- x' region in detail and in this experiment we are able to extend into this region for small values of q^2 . Using the method described in Sec. II G, we extract the smeared neutron cross section σ_n^S . We present results in terms of σ_n^S/σ_p^S . This quantity is essentially the same as σ_n/σ_p for our data, since the smearing ratios for the proton and neutron are small and

TABLE VI. Elastic electron-proton cross sections. Both the statistical errors and the estimated systematic errors are shown. The systematic errors are obtained by adding in quadrature the 2.62% error estimated in Table V to a 1% error estimated in the radiative correction procedure.

E_0 (GeV)	q^2 [(GeV/c) ²]	$d\sigma/d\Omega$ ($\mu\text{b}/\text{sr}$)	Systematic error ($\mu\text{b}/\text{sr}$)
4.500	0.098	110.80 \pm 0.49	\pm 3.10
7.001	0.235	30.164 \pm 0.065	\pm 0.846
9.993	0.474	7.641 \pm 0.025	\pm 0.214
13.000	0.797	2.2151 \pm 0.0046	\pm 0.0620
16.000	1.198	0.7136 \pm 0.0041	\pm 0.020
18.010	1.510	0.3473 \pm 0.0028	\pm 0.0097
20.005	1.853	0.1778 \pm 0.0011	\pm 0.0050

the effects of this correction tend to cancel in the ratio.

We first look at the quantity $\sigma_D/\sigma_p^S = 1 + \sigma_n^S/\sigma_p^S$ as a function of q^2 for different regions of x' . Plots of this quantity are shown in Fig. 16. We see that "scaling" of σ_D/σ_p^S (that is, no dependence upon q^2) begins at low values of q^2 . Using the "closure approximation" to take into account the nuclear elastic scattering (see Ref. 15 and Appendix B) suggests a q^2 variation in the cross section of the form $\sigma_D \propto 1 - |F_d(q^2)|^2$, where F_d is the deuteron elastic form factor.²⁵ For the lower- x' bins, where the data extend to low q^2 , there is a variation consistent with this behavior. We fitted the ratio σ_D/σ_p^S for each x' bin to the form $A(1 - |F_d(q^2)|^2)$ and these fits are shown on the graphs. We point out that only data for $W > 2.1$ GeV have been used in these fits to avoid the resonance region. From each of these fits, we have extracted a value of A and its error and listed the quantities $(A - 1)$ in Table VII. These values represent the neutron-proton ratio σ_n^S/σ_p^S for each bin, since, except for the two lowest ranges of x' , A is essentially the average of the measurements in that bin. These two values for the two lowest ranges of x' are obtained from extrapolation into the scaling region from data measured at $q^2 \leq 0.75$ (GeV/c)². These extracted values for σ_n^S/σ_p^S are plotted in Fig. 17 along with results from larger angles.^{24, 26} The differences in σ_n/σ_p between the three experiments correspond to $\approx 3\%$ differences in the σ_D/σ_H measurements and are comparable with the estimated systematic errors in the three experiments. Assuming that $R = \sigma_L/\sigma_T$ is the same for the neutron and proton, then for large ω' (where the smearing ratio is near unity)

$$\begin{aligned} \frac{\sigma_D}{\sigma_p^S} - 1 &= \frac{\sigma_n^S}{\sigma_p^S} \\ &= \frac{W_{2n}^S}{W_{2p}^S} \\ &= \frac{W_{2n}}{W_{2p}}. \end{aligned} \quad (12)$$

It is expected that purely diffractive processes should dominate as $\omega' \rightarrow \infty$ so that σ_n/σ_p should approach 1. In these data the ratio obtained from the two extrapolated points at lowest x' are consistent with 1. It is of some interest that the ratio is significantly below 1 for $x' \geq 0.05$ ($\omega' \sim 20$). Recall that there is an estimated uncertainty of $\pm 1.57\%$ in σ_D/σ_H which becomes $\sim 3\%$ in σ_n/σ_p . Systematic errors from the radiative corrections tend to cancel in this ratio and have an appreciable effect in only the two lowest ranges of x' . These two points are in a kinematic region where there

are no measurements of A dependence (see Sec. IV F) and further uncertainty can arise from our neglect of shadowing corrections.

C. νW_2 for the proton and the approach to scaling

The experimental observation of scaling of the structure function νW_2 has been observed¹ for some region of q^2 and W . The original scaling variable of Bjorken, ω , has been supplemented by several others to extend the range of kinematic variables where scaling works. We use the variable $\omega' = 1 + W^2/q^2$, where $\nu W_2(\omega')$ has previously been shown to exhibit scaling behavior for values of $q^2 \geq 2$ (GeV/c)² and outside the resonance region of $W \geq 2$ GeV. Since W_2 vanishes at $q^2 = 0$, it is an interesting question to see how νW_2 approaches its scaling behavior. In Fig. 18 we show νW_2

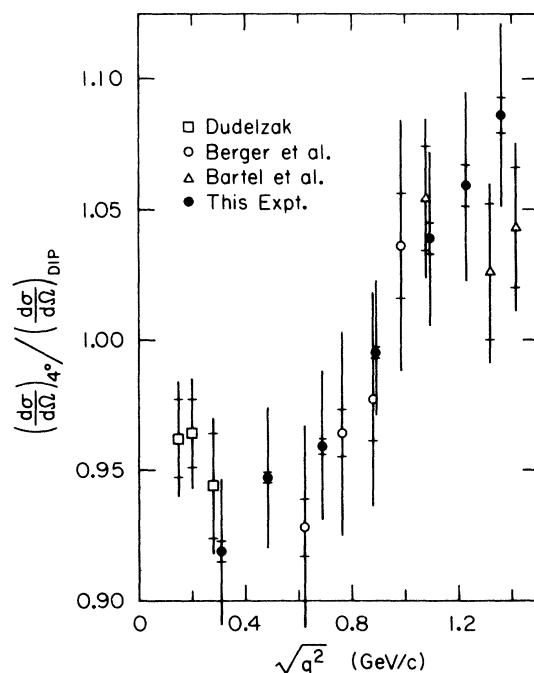


FIG. 15. The ratio of the measured elastic electron-proton cross section $d\sigma/d\Omega$ to the cross section calculated using the dipole approximation for the electric form factor $G_E = (1 + q^2/0.71)^{-2}$, form-factor scaling to yield the magnetic form factor $G_M = 2.793G_E$, and the Rosenbluth (Ref. 23) approximation to the elastic cross section. Statistical errors for this experiment are shown by the inner error bars. The extended lines show the estimated systematic errors. The other points are deduced from fits to the Rosenbluth cross section extrapolated to 4° . The inner error bars on these points represent the errors derived from the fits with statistical errors on the data. The extended lines show the systematic errors quoted by the authors added in quadrature with the statistical errors.

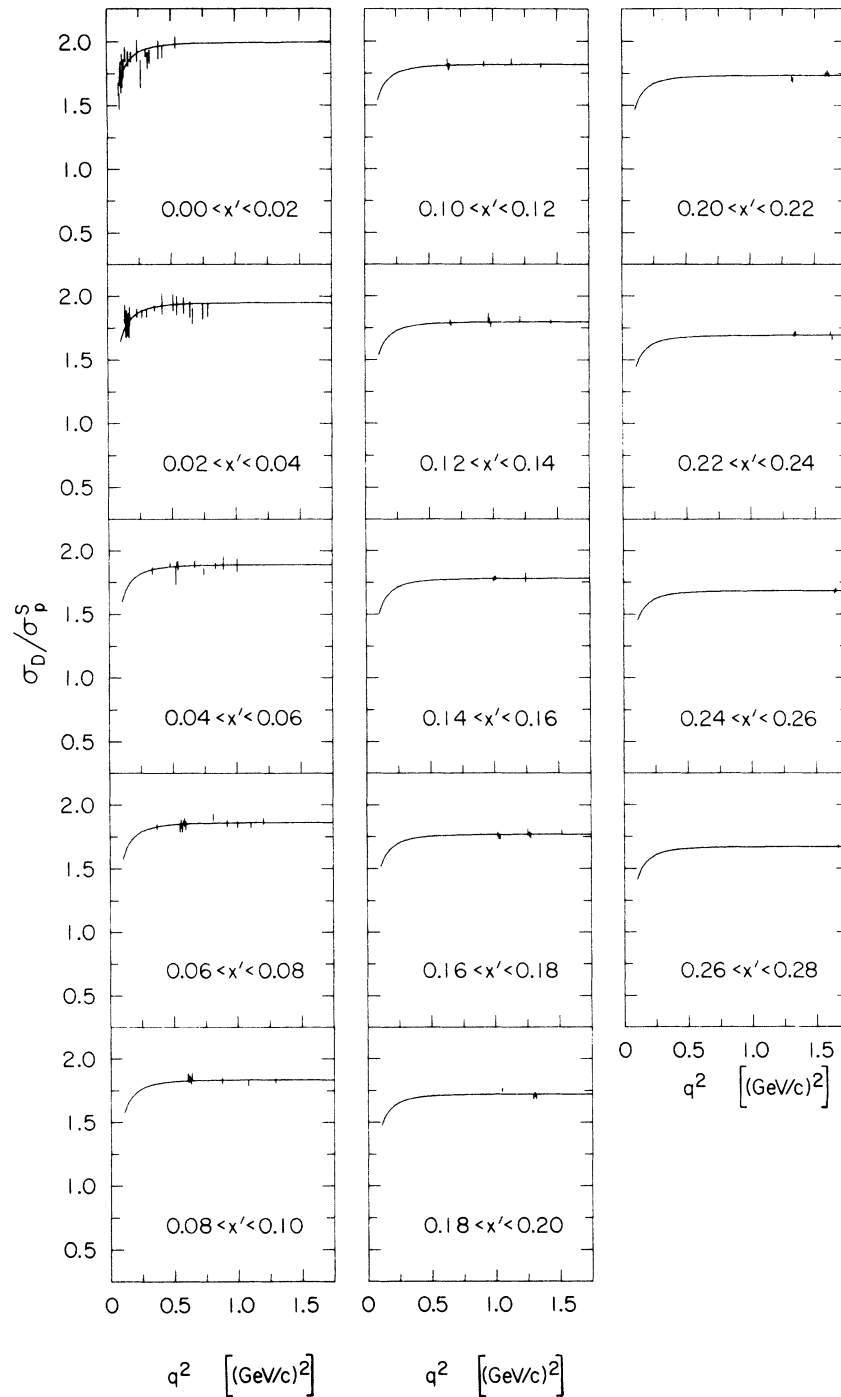


FIG. 16. The ratio of the deuterium cross section to the smeared proton cross section vs q^2 for different ranges of x' as shown. The curves are the functions $A[1 - |F_d(q^2)|^2]$, where values of A are determined from fits to each set of data, and F_d is the deuteron elastic form factor from Ref. 25. For all points W is greater than 2.1 GeV.

versus q^2 for $\omega' > 6$. Only data for $W > 2$ GeV are used, and we have assumed $R = \sigma_L / \sigma_T = 0.18$. As stated earlier, the largest effect due to uncertainties in R occurs for the largest ω' values (lowest q^2). These data suggest that the turn-on to scaling depends mostly on q^2 . Vector-meson dominance is expected to apply for large values of ω' (small values of q^2 in this experiment) and in this region will predict that νW_2 depends mainly on q^2 .

By analogy with the situation in deuterium where the inelastic cross section is suppressed by the coherent nuclear elastic scattering, we parametrize the inelastic structure function W_2 for the proton as a product:

$$\nu W_{2p}(q^2, \nu) = [1 - W_2^{\text{el}}(q^2)] F_{2p}(\omega'), \quad (13)$$

where $F_{2p}(\omega')$ is the scaling limit structure function and

$$W_2^{\text{el}}(q^2) = \frac{G_E^2(q^2) + \tau G_M^2(q^2)}{1 + \tau}, \quad \tau = \frac{q^2}{4M^2} \quad (14)$$

is the counterpart of W_2 for elastic scattering (see Appendix B), where G_E and G_M are, respectively, the elastic electric and magnetic form factors for the proton. This form satisfies the constraint that W_2 vanish at $q^2 = 0$. Integrating W_{2p} over all values of ν yields

$$\int_{\text{inelastic}} d\nu W_{2p}(q^2, \nu) = [1 - W_2^{\text{el}}(q^2)] \int_{\text{inelastic}} \frac{d\nu}{\nu} F_{2p}(\omega'). \quad (15)$$

But this is the Gottfried sum rule²⁷ for the proton,

TABLE VII. Neutron-proton ratios. A is determined from the fit to $\sigma_D / \sigma_p^S = A[1 - |F_d(q^2)|^2]$. The first error shown is from the fit. In the right-hand column we give estimates of the systematic errors. These are computed by combining in quadrature the $\pm 1.57\%$ systematic error in σ_D / σ_p^S with the estimate of radiative correction errors given in Sec. II F

Bin	$(A - 1)$	Systematic errors
0 < x' < 0.02	0.994 \pm 0.0125	\pm 0.053
0.02 < x' < 0.04	0.949 \pm 0.0096	\pm 0.036
0.04 < x' < 0.06	0.892 \pm 0.0089	\pm 0.031
0.06 < x' < 0.08	0.862 \pm 0.0074	\pm 0.030
0.08 < x' < 0.10	0.839 \pm 0.0084	\pm 0.030
0.10 < x' < 0.12	0.822 \pm 0.0089	\pm 0.030
0.12 < x' < 0.14	0.797 \pm 0.0077	\pm 0.029
0.14 < x' < 0.16	0.781 \pm 0.0096	\pm 0.029
0.16 < x' < 0.18	0.769 \pm 0.0067	\pm 0.029
0.18 < x' < 0.20	0.724 \pm 0.0089	\pm 0.028
0.20 < x' < 0.22	0.736 \pm 0.0073	\pm 0.028
0.22 < x' < 0.24	0.692 \pm 0.0077	\pm 0.028
0.24 < x' < 0.26	0.685 \pm 0.0096	\pm 0.028
0.26 < x' < 0.28	0.672 \pm 0.0121	\pm 0.027

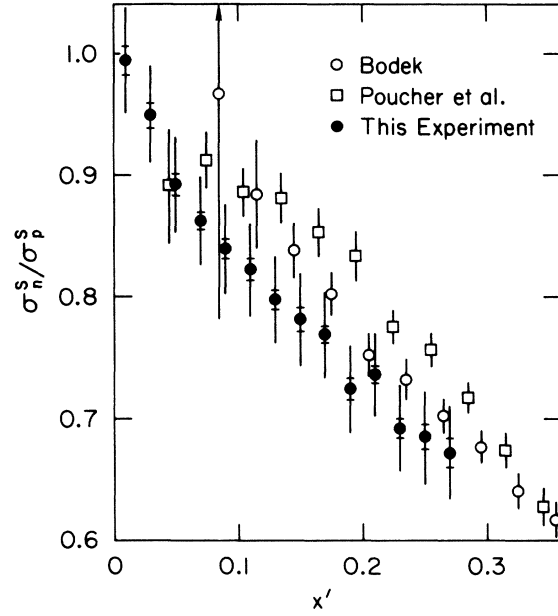


FIG. 17. Experimental measurements of the smeared neutron-proton ratio, σ_n^S / σ_p^S vs x' . For this experiment, statistical errors are shown by the inner error bars. The extended lines represent estimates of the systematic errors. No corrections have been made for any possible A dependence in deuterium. The other data are from Refs. 24 and 26, the error bars do not include estimated systematic errors of about $\pm 6\%$.

where

$$\int_{\text{inelastic}} \frac{d\nu}{\nu} F_{2p}(\omega') = \sum_i q_i^2 \quad (16)$$

is the sum of the parton charges squared.

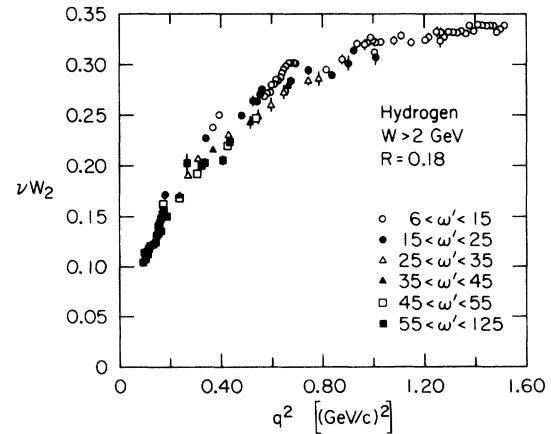


FIG. 18. Extracted values of νW_2 for the proton vs q^2 . Only data with $W > 2$ GeV and $\omega' > 6$ have been used and $R = \sigma_L / \sigma_T = 0.18$ has been assumed. The errors are statistical only.

In order to examine the factorization parametrization, we have separated the data into equal bins of ω' and included some earlier measurements²⁴ at 6° and 10°. The data in each bin are plotted as a function of q^2 in Fig. 19. The curves shown are fits to

$$\nu W_{2p}(q^2, \text{fixed } \omega') = D(\omega')[1 - W_2^{\text{cl}}(q^2)], \quad (17)$$

where D was determined for each bin of ω' separately. The values of D with the errors from the fit and an estimate of the systematic errors are listed in Table VIII. Thus we see that the turn-on to scaling is adequately accounted for by the factorization parametrization. Using the results of the fits for each ω' bin we estimate the values of $F_{2p}(\omega')$ for larger values of ω' than previously available. In Fig. 20 we have plotted νW_{2p} versus ω' obtained this way. The region at low $\omega' < 5$ is obtained from a larger-angle experiment.¹² The values obtained from the various fits in the present experiment are shown starting at $\omega' = 8$. We should point out that for $\omega' > 32$ the results of the fit will depend upon the factorization parametrization more and more strongly as ω' gets larger, since the range of q^2 for the data gets quite limited. We can then refit both the small and large ω' regions to the form

$$F_{2p}(\omega') = \sum_{n=3}^7 a_n (1 - 1/\omega')^n \quad (18)$$

and obtain the values

$$\begin{aligned} a_3 &= 1.0621, \\ a_4 &= -2.2594, \\ a_5 &= 10.5400, \\ a_6 &= -15.8277, \\ a_7 &= 6.7931, \end{aligned} \quad (19)$$

with $F_{2p}(\infty) = 0.308$. We emphasize that the systematic uncertainties may be as large as 20% by the highest ω' bin, so the results for these parameters must be used with caution.

D. Resonances in electron-proton scattering

Perhaps the most obvious feature of the data in this range of q^2 is the production of the nucleon resonances [see Fig. 10(a)]. There are four enhancements in the scattering cross sections which will be referred to as the first, second, third, and fourth resonance regions. If we look at results from photoproduction,²⁸ we know that these regions, except for the first, contain several resonances each.

There is no obvious evidence of enhancements above $W = 2$ GeV. We have fitted the data between

$W = 2$ and 3 GeV to quadratics in W for each of five energies. Figure 21 shows the residuals of the fits. These data are consistent with no enhancements. At an incident energy of 13 GeV, a resonance with a strength of 3% of the first resonance

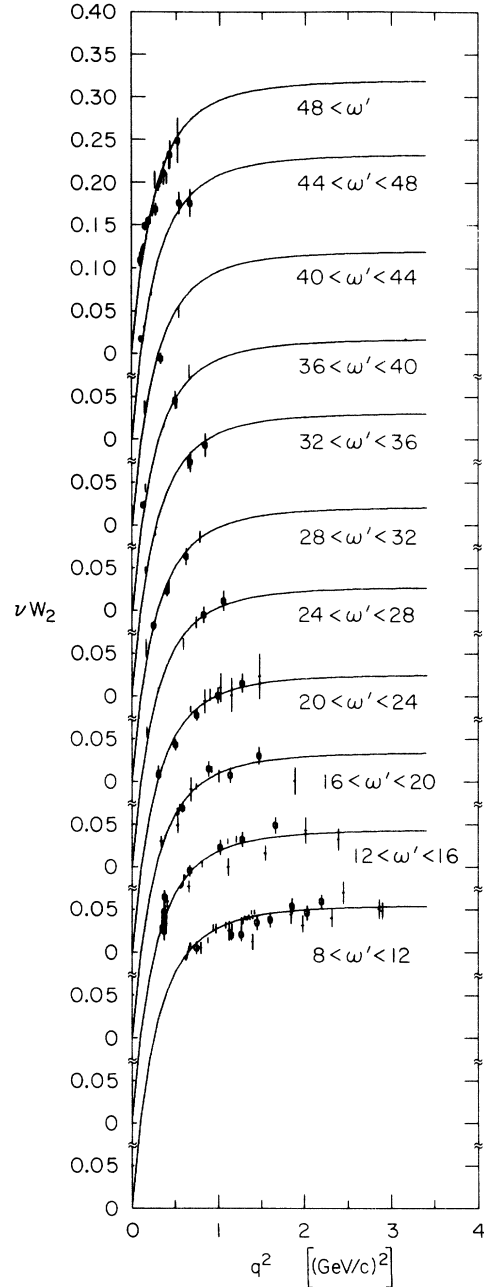


FIG. 19. Extracted values of νW_2 vs q^2 for the proton, assuming $R = 0.18$. The separate ω' ranges are shown. The open circles are 6° data and the dashes are 10° data, both from Ref. 24. The curves are the functions $D[1 - W_2^{\text{cl}}(q^2)]$ with values of D determined from fits to each set of data separately.

TABLE VIII Extracted structure function. Values of D determined from the fits to νW_2 for each ω' bin. The first errors shown are from the fit. The errors listed under ΔR arise from uncertainties in R and are obtained by letting $R=0$ and comparing to the results with $R=0.18$. The extrapolation error assigned corresponds to $\frac{1}{2}$ of the difference of the function evaluated at the asymptotic value and at the q^2 of the last measured data point for that bin. These three sources of error are then combined in quadrature and the result listed under combined error. There is also the over-all $\pm 2.62\%$ systematic uncertainty (see Table VI). There is an additional systematic error from the radiative corrections of $3-7.5\%$ which is larger for higher ω' .

Bin	D	ΔR	Extrapolation error	Combined error
$8 < \omega' < 12$	0.355 ± 0.0005	± 0.004	± 0.001	± 0.0042
$12 < \omega' < 16$	0.343 ± 0.0008	± 0.005	± 0.002	± 0.0054
$16 < \omega' < 20$	0.335 ± 0.0012	± 0.006	± 0.003	± 0.0068
$20 < \omega' < 24$	0.325 ± 0.0014	± 0.009	± 0.006	± 0.0109
$24 < \omega' < 28$	0.328 ± 0.0029	± 0.010	± 0.011	± 0.0151
$28 < \omega' < 32$	0.321 ± 0.0031	± 0.011	± 0.018	± 0.0213
$32 < \omega' < 36$	0.332 ± 0.0027	± 0.009	± 0.017	± 0.0194
$36 < \omega' < 40$	0.317 ± 0.0022	± 0.013	± 0.023	± 0.0265
$40 < \omega' < 44$	0.320 ± 0.0051	± 0.018	± 0.031	± 0.0362
$44 < \omega' < 48$	0.332 ± 0.0030	± 0.011	± 0.024	± 0.0266
$48 < \omega'$	0.319 ± 0.0014	± 0.020	± 0.031	± 0.0369

and a similar width would be easily observed in the graph of the residuals. The sensitivity decreases rapidly with increasing q^2 .

To study the four prominent enhancements between $W=1.07$ and 2 GeV, we have adopted the following procedure: The measured cross sections were first converted to a virtual photoabsorption cross section

$$\begin{aligned} \sigma_{\text{tot}}(q^2, W) &\equiv \frac{1}{\Gamma_T} \frac{d^2\sigma}{d\Omega dE'} = \sigma_T + \epsilon\sigma_L \\ &= \sigma_R(q^2, W) + \sigma_{\text{bkd}}(q^2, W), \end{aligned} \quad (20)$$

where σ_R and σ_{bkd} are the resonance and background contributions to the cross sections. In order to remove some of the known kinematic variations, we write the structure function νW_2 as

$$\begin{aligned} \nu W_2(q^2, W) &= [1 - W_2^{\text{el}}(q^2)] F_2(\omega') B(q^2, W) \\ &\times \left[4\pi^2 \alpha F_2(\infty) \lim_{q^2 \rightarrow 0} \frac{1 - W_2^{\text{el}}(q^2)}{q^2} \right]^{-1} \end{aligned} \quad (21)$$

where the term in the large square brackets is included so that

$$\lim_{q^2 \rightarrow 0} B(q^2, W) = \sigma_{\gamma p}(W) \quad (22)$$

and $\sigma_{\gamma p}(W)$ is the total photoproduction cross section. This makes

$$\begin{aligned} B(q^2, W) &= \left[\frac{q^2}{1 - W_2^{\text{el}}(q^2)} \lim_{q^2 \rightarrow 0} \frac{1 - W_2^{\text{el}}(q^2)}{q^2} \right] \\ &\times \left(\frac{\nu K}{q^2 + \nu^2} \right) \left(\frac{1+R}{1+\epsilon R} \right) \left[\frac{F_2(\infty)}{F_2(\omega')} \right] \sigma_{\text{tot}}(q^2, W), \end{aligned} \quad (23)$$

where we have used $R=0.23q^2$ which has the cor-

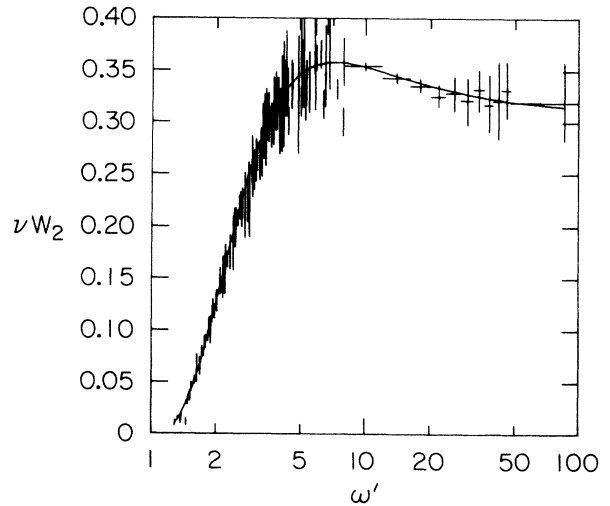


FIG. 20. The points below $\omega' = 8$ are values of νW_2 for the proton from Ref. 12. The data above $\omega' = 8$ are the values of D shown in Table VIII. The solid line is a fit to all the data shown using statistical errors on the data only.

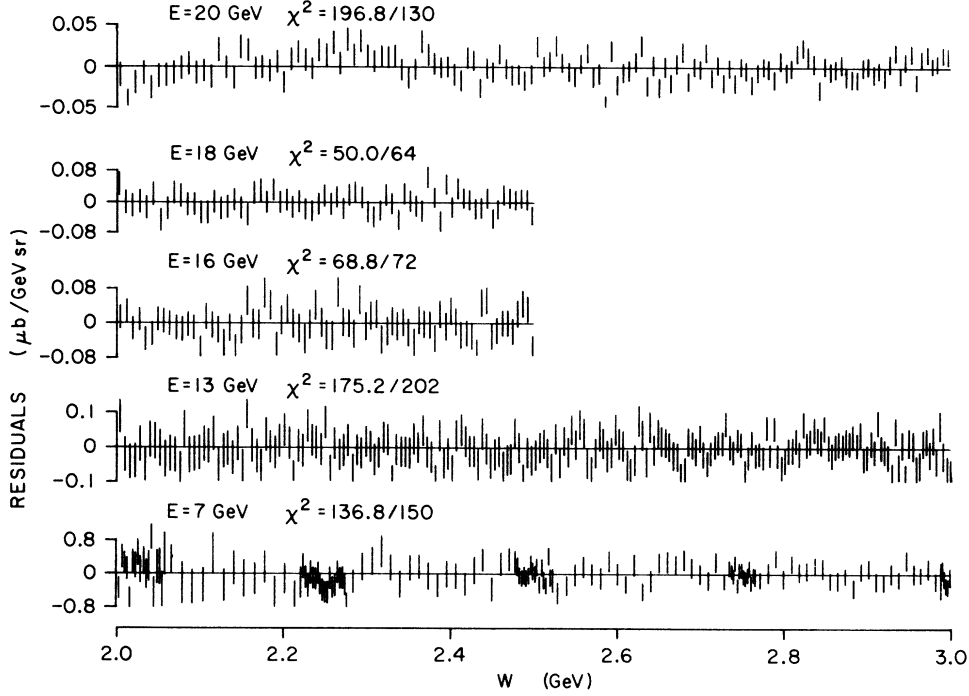


FIG. 21. The residuals from the quadratic fits to the cross section for the range $2 < W < 3$ GeV for each energy. The $\chi^2/\text{degree of freedom}$ for each fit is shown.

rect limit as $q^2 \rightarrow 0$ and is consistent with electroproduction data²⁹ for $q^2 < 2$ (GeV/c)².

We then fitted the values of B for each of the lines separately to the sum of four resonances and a polynomial background, only including data for $W \leq 2.1$ GeV:

$$B(q^2, W) = \sum_{i=1}^4 \text{Res}_i(q^2, W) + \sum_{j=1}^4 c_j q^{*j}, \quad (24)$$

where

$$q^* = \{[(W^2 + M^2 - m_\pi^2)/2W]^2 - M^2\}^{1/2}. \quad (25)$$

For single-pion production, q^* is the momentum of the pion in the πN c.m. system. The resonance forms used were the same as in Walker's analysis of photoproduction²⁸:

$$\text{Res}_i(q^2, W) = A_R \left(\frac{k_R^*}{k^*} \right)^2 W_R^2 \frac{\Gamma \Gamma_\gamma}{(W_R^2 - W^2)^2 + W_R^2 \Gamma^2}, \quad (26)$$

where

$$k^* = \{[(W^2 + M^2 + q^2)/2W]^2 - M^2\}^{1/2} \quad (27)$$

is the momentum of the virtual photon in the same πN c.m. system,

$$k_R^* = k^* \text{ at } W = W_R, \quad (28)$$

$$\Gamma = \Gamma_R \left(\frac{q^*}{q_R^*} \right)^{2L+1} \left(\frac{q_R^{*2} + X^2}{q^{*2} + X^2} \right)^L, \quad (29)$$

and

$$\Gamma_\gamma = \Gamma_R \left(\frac{k^*}{k_R^*} \right)^{2J} \left(\frac{k_R^{*2} + X^2}{k^{*2} + X^2} \right)^J. \quad (30)$$

The parameters that were fitted for each resonance region were the amplitude A_R , mass W_R , and width Γ_R . The other parameters L , J , and X were taken from Walker and are shown in Table IX. For some lines, the fourth resonance enhancement was omitted from the fit, and for others, some parameters were held fixed to stabilize the fit. Table X lists the results of the fits for each

TABLE IX. Resonance region assignments. Spin assignments are taken from Ref. 28. X is the parameter determining the mass variation of the width.

Resonance region	L	J	X (GeV)	Identified with
1	1	1	0.160	$P_{33}(1236)$
2	2	1	0.350	$D_{13}(1520)$
3	3	2	0.350	$F_{15}(1688)$
4	3	2	0.350	$F_{37}(1950)$

TABLE X. Resonance-fit parameters (A_R , W_R , and Γ_R) and background-fit parameters (C_1 , C_2 , C_3 , and C_4). The errors shown are the results from the error matrix from the fit. If no error is shown, the parameter was held fixed. If no value is shown, the parameter was omitted from the fit.

E_0 (GeV)	4.5	7	10	13	16	18	20
Region 1							
A_R (μb)	289.7 \pm 4.05	221.3 \pm 1.50	167.1 \pm 1.15	137.7 \pm 0.75	118.8 \pm 1.82	104.5 \pm 2.32	93.79 \pm 1.87
W_R (GeV)	1.227 \pm 0.0010	1.231 \pm 0.0005	1.225 \pm 0.0006	1.224 \pm 0.0004	1.226 \pm 0.0010	1.233 \pm 0.0015	1.236 \pm 0.0015
Γ_R (GeV)	0.116 \pm 0.0040	0.123 \pm 0.0021	0.119 \pm 0.0027	0.119 \pm 0.0016	0.120 \pm 0.0046	0.124 \pm 0.0068	0.141 \pm 0.0071
Region 2							
A_R (μb)	118.2 \pm 3.82	100.8 \pm 1.70	82.94 \pm 1.61	72.52 \pm 0.82	70.62 \pm 1.70	62.06 \pm 2.20	61.15 \pm 1.70
W_R (GeV)	1.519 \pm 0.0025	1.516 \pm 0.0010	1.512 \pm 0.0010	1.509 \pm 0.0005	1.507 \pm 0.0009	1.511 \pm 0.0012	1.513 \pm 0.0009
Γ_R (GeV)	0.144 \pm 0.010	0.130 \pm 0.0046	0.114 \pm 0.0043	0.097 \pm 0.0021	0.088 \pm 0.0040	0.077 \pm 0.0052	0.078 \pm 0.0042
Region 3							
A_R (μb)	64.92 \pm 3.74	61.56 \pm 1.67	61.06 \pm 1.93	57.32 \pm 1.01	51.18 \pm 1.64	50.79 \pm 2.18	47.00 \pm 1.75
W_R (GeV)	1.675 \pm 0.0031	1.681 \pm 0.0014	1.692 \pm 0.0016	1.696 \pm 0.0008	1.700 \pm 0.0013	1.705 \pm 0.0017	1.713 \pm 0.0014
Γ_R (GeV)	0.113 \pm 0.014	0.102 \pm 0.0055	0.115 \pm 0.0071	0.105 \pm 0.0035	0.094 \pm 0.0061	0.092 \pm 0.0079	0.102 \pm 0.0072
Region 4							
A_R (μb)	21.87 \pm 4.13	12.57 \pm 1.59	10.26 \pm 2.08	13.71 \pm 3.14	11.78 \pm 2.49
W_R (GeV)	1.950	1.950	1.950	1.950	1.950
Γ_R (GeV)	0.200	0.200	0.200	0.200	0.200
C_1 ($\mu\text{b}/\text{GeV}$)	351.2 \pm 36.8	167.2 \pm 13.4	186.2 \pm 14.3	164.6 \pm 14.3	164.6 \pm 8.07	185.3 \pm 19.5	54.0 \pm 24.8
C_2 ($\mu\text{b}/\text{GeV}^2$)	- 926.5 \pm 268.2	- 364.3 \pm 98.7	- 481.4 \pm 103.3	- 316.4 \pm 53.14	- 316.4 \pm 53.14	- 333.4 \pm 115.1	320.3 \pm 124.1
C_3 ($\mu\text{b}/\text{GeV}^3$)	1857.6 \pm 623.5	1270.2 \pm 221.2	1323.5 \pm 247.1	912.1 \pm 122.1	912.1 \pm 122.1	879.5 \pm 236.5	-482.9 \pm 264.9
C_4 ($\mu\text{b}/\text{GeV}^4$)	-1191.0 \pm 440.4	-1017.1 \pm 147.7	-1011.9 \pm 175.5	-681.2 \pm 83.7	-681.2 \pm 83.7	-651.6 \pm 150.4	204.4 \pm 173.0

line. In addition, we have fitted the total photoproduction data³⁰ to the same form. In Fig. 22 we show the data and the fitted functions.

We recognize that assigning only one Breit-Wigner resonant shape to each of the four obvious enhancement regions may be an oversimplified representation of the actual physics underlying the enhancements. For example, in Fig. 22 it is evident that in the third resonance region the mass at the peak of the enhancement increases as the incident energy increases. This is borne out by the fits given in Table X, where W_R increases continuously from 1675 to 1713 MeV as q^2 increases from 0.08 to 1.8 GeV². Fits with two, instead of one, Breit-Wigner shapes in the third resonance region are consistent, not surprisingly, with a lower-mass resonance (around 1670 MeV) decreasing in amplitude as q^2 increases plus a higher-mass resonance (around 1710 MeV) increasing as q^2 increases. However, considering the various arbitrary aspects of the parametrization used in fitting, we have not pursued a more detailed breakdown of the total cross section into its constituent reactions. In deuterium there is an extra complication due to smearing, and we are not presenting an analysis of the resonant structures for this target.

After the parameters were determined from the fits, the amplitudes A_R , were converted to values of $\sigma_{\text{res}} = \sigma_R(W = W_R)$ for each resonance separately. These values are listed with their corresponding values of q^2 in Table XI. In addition, for the first resonance we have calculated the expected value of σ_{res} , assuming the form used by Bartel *et al.*,³¹ in analyzing the first resonance data. This predicts that at the resonant mass, the cross section is

$$\sigma_{\text{res}} = \frac{4\alpha\pi(\nu^2 + q^2)}{\Gamma_0 W_R (W_R^2 - M^2)} \left[\frac{G_M^*(q^2)}{G_D(q^2)} \right]^2 G_D^2(q^2), \quad (31)$$

where

$$\Gamma_0 = 115 \text{ MeV}$$

and

$$G_D(q^2) = 3/(1 + q^2/0.71)^2. \quad (32)$$

This determines the ratio $(G_M^*/G_D)^2$ and these values are listed in Table XII for the first resonance. In Fig. 23 we plot this ratio for our data and the previous DESY experiment. Our results are consistent with the others that show this form factor definitely falls off faster than the dipole expression in this q^2 range.

The results for σ_{res} for each of the resonance regions are shown in Fig. 24. The slope of a line through the data is clearly greater for the first resonance than for any of the others. The second,

third, and fourth regions exhibit similar behavior as q^2 increases, whereas the first resonance amplitude is decreasing more rapidly. In Fig. 25, we have also plotted the ratio of the resonance peak height to the amount of background at the peak as determined from the fit. This shows that, whereas the first resonance becomes smaller compared with the background as q^2 increases, the higher-mass resonances show less dependence on q^2 .

As can be observed in the photoproduction data (see Fig. 22), there is some evidence for an enhancement in the region of $W = 1435$. This can be attributed to the $P_{11}(1470)$ and is normally included in fits to photoproduction data.³⁰ In our electroproduction data, satisfactory fits can be obtained without assuming any resonance in this mass region.

E. Sum rules

Over the ranges of the experimental data we calculate integrals occurring in certain sum rules.

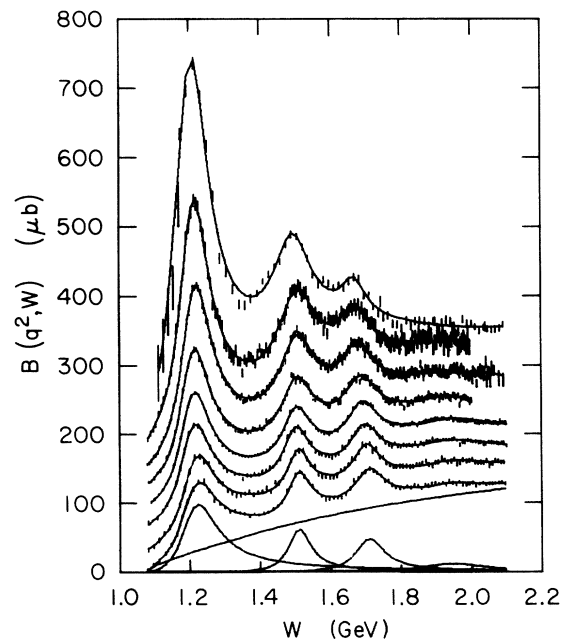


FIG. 22. Measured values of $B(q^2, W)$ (see text) vs missing mass W . The curves show the fit and typical contributions of the resonances and background. Each lower energy line is offset upward by $30 \mu\text{b}$. The top line is photoproduction data of Ref. 30 offset by $210 \mu\text{b}$. The succeeding lines are the data from the current experiment for 4.5, 7, 10, 13, 16, 18, and 20 GeV. The curves along the bottom axis show the decomposition of the 20-GeV line into the contributions from the individual resonances and the background.

TABLE XI. Resonance amplitudes. The amplitudes of each resonance-region cross section σ_{res} at the corresponding resonance mass. The first errors shown are the fit errors. We also estimate the error due to the particular parametrization used in the fit by assuming a different parametrization could result in the background varying by as much as $\pm 10\%$.

	q^2 [(GeV/c) ²]	σ_{res} (μb)	Error from fit parametrization
First resonance region	0.09	505.0 \pm 7.06	\pm 8.75
	0.22	468.7 \pm 3.19	\pm 6.68
	0.46	327.2 \pm 2.95	\pm 5.82
	0.78	187.7 \pm 1.03	\pm 4.00
	1.17	98.02 \pm 1.50	\pm 2.72
	1.48	59.12 \pm 1.31	\pm 1.88
	1.82	36.48 \pm 0.73	\pm 1.32
Second resonance region	0.08	129.5 \pm 4.19	\pm 10.1
	0.21	113.8 \pm 1.92	\pm 8.63
	0.44	84.24 \pm 1.63	\pm 6.67
	0.75	57.07 \pm 0.65	\pm 5.11
	1.14	38.84 \pm 0.94	\pm 3.79
	1.44	25.89 \pm 0.92	\pm 3.14
	1.78	19.12 \pm 0.53	\pm 2.25
Third resonance region	0.08	65.87 \pm 3.79	\pm 11.8
	0.20	60.29 \pm 1.64	\pm 10.2
	0.43	51.52 \pm 1.63	\pm 7.50
	0.73	37.73 \pm 0.66	\pm 5.89
	1.12	24.47 \pm 0.78	\pm 4.46
	1.42	19.11 \pm 0.82	\pm 3.59
Fourth resonance region	1.75	13.74 \pm 0.51	\pm 2.72
	0.40	15.98 \pm 3.02	\pm 7.82
	0.70	7.18 \pm 0.91	\pm 6.51
	1.08	4.39 \pm 0.89	\pm 4.95
	1.38	4.76 \pm 1.09	\pm 3.91
1.71	3.29 \pm 0.70	\pm 3.10	

First, there is the Callan-Gross³² integral:

$$I_{1p} = \int_1^\infty \frac{d\omega}{\omega^2} \nu W_2$$

$$= \int_0^1 dx F_{2p}(x). \quad (33)$$

In the parton model, I_{1p} represents the mean

TABLE XII. First resonance transition form factor. Values of the transition form factor G_{Δ}^* compared to a dipole form $G_D(q^2) = 3/(1 + q^2/0.71)^2$. The errors include the fit error added linearly to the fit-parametrization error estimate.

q^2 [(GeV/c) ²]	$[G_{\Delta}^*(q^2)/G_D(q^2)]^2$
0.09	0.950 \pm 0.030
0.22	0.905 \pm 0.019
0.46	0.828 \pm 0.022
0.78	0.735 \pm 0.020
1.17	0.633 \pm 0.027
1.48	0.548 \pm 0.030
1.82	0.475 \pm 0.027

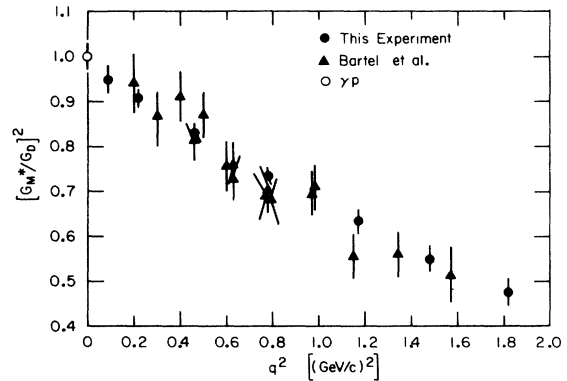


FIG. 23. Measured values of the transition form factor for $\Delta(1238)$ production compared to the dipole $G_D(q^2) = 3/(1 + q^2/0.71)^2$ vs q^2 . The open circle is from a fit to photoproduction data of Ref. 30. The other measurements are from Ref. 31.

square charge per parton. We also calculate the Gottfried integral²⁷:

$$I_{2p} = \int_1^\infty \frac{d\omega}{\omega} \nu W_2$$

$$= \int_0^1 \frac{dx}{x} F_{2p}(x). \quad (34)$$

In the parton model, this represents the sum of the squares of the parton charges in the proton.

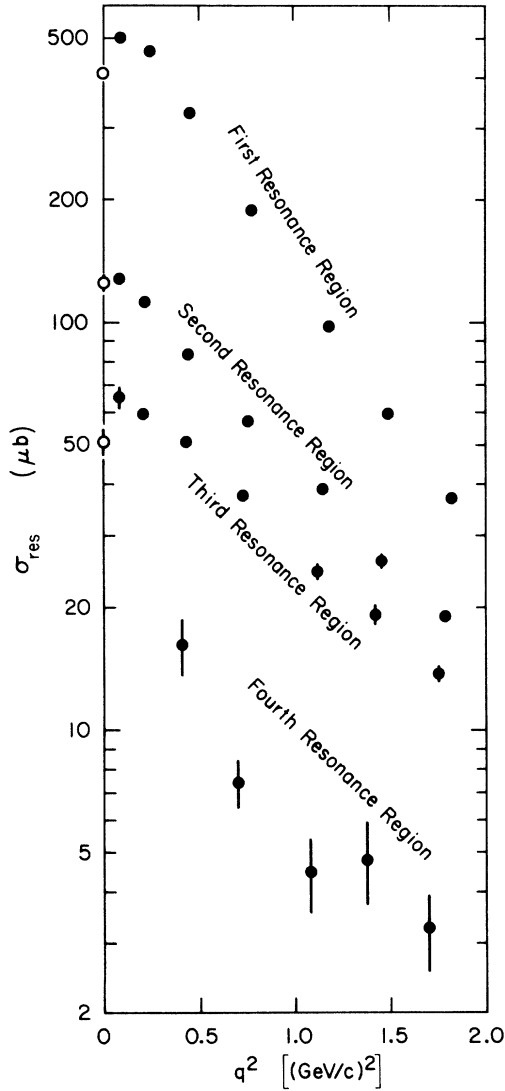


FIG. 24. Measured values of the cross section from the resonances evaluated at each resonance mass vs q^2 . The open circles are from fits to photoproduction data of Ref. 30. Errors are statistical only.

In Table XIII we list the measured values of these integrals and their expected values in the three-quark model and in a simple parton model.³³ For convenience we evaluated the integrals using the fit to $F_{2p}(x')$ given in Sec. IV C and shown in Fig. 20. Since the variable x' is observed to be a better scaling variable for the finite q^2 where data are available, we have used $F_{2p}(x')$ as an estimate of the asymptotic scaling function $F_{2p}(x)$ and have calculated all the integrals in terms of x' . By combining the results of the fit for $F_{2p}(x')$ with the measured σ_n/σ_p ratio, we calculate the corresponding integrals for the difference between proton and neutron. For values of $x' > 0.28$, we have used the data from Ref. 26. Remember that there are no data for $x' < 0.02$ and also there are no data in the scaling region for $x' < 0.05$, and that these regions may be important for the I_{2p} and I_{2n} integrals. Note that the errors given in Table XIII are the estimated systematic errors. Propagation of the statistical errors yields values much smaller than the errors shown. An interesting discussion of the significance of these sum rules is given in Ref. 34.

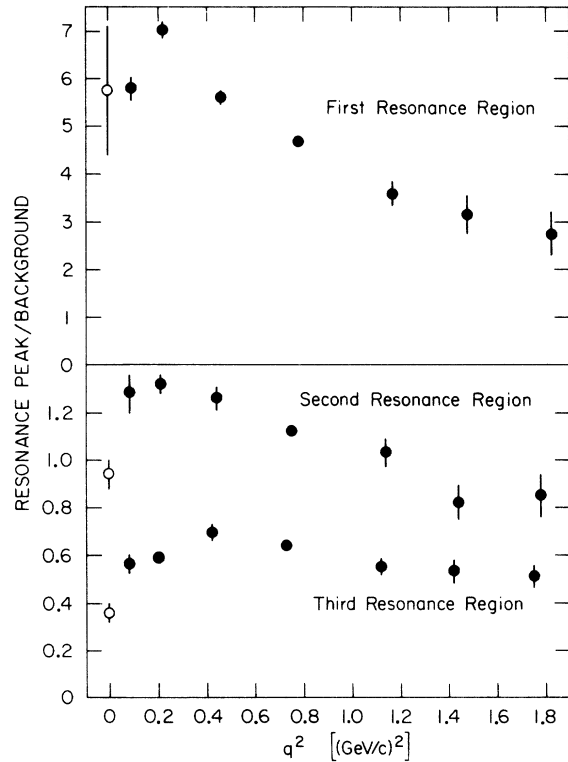


FIG. 25. Measured values of the ratio of resonance-peak cross sections to the background at each peak as determined from the fits. The open circles are from fits to photoproduction (Ref. 30).

F. *A* dependence

The phenomenon of "shadowing," in which the scattering probability per nucleon decreases in heavy nuclei, has been observed³⁵ in purely hadronic processes, such as πA scattering, and also in photoproduction. The usual explanation relies on the fact that the mean free path for hadronic interactions is of the same order as the nuclear sizes, so the incident particle is only able to see the surface of the nucleus. This would give a cross section of $\sigma_A = \sigma_0 A^{2/3}$. In photoproduction, where a naive estimate gives a mean free path large compared to the nuclear size, models like vector dominance, in which the photon spends some of the time as a hadron, can be used to account for the observed shadowing. However, previous experiments in electroproduction have failed to show any shadowing effect.⁴

In this experiment, we took data on targets of hydrogen, deuterium, beryllium, aluminum, copper, and gold at energies of 13 and 20 GeV in order to see if any *A* dependence could be observed for low q^2 electroproduction. The analysis for the targets heavier than deuterium was done in the same way as for deuterium, except that no smearing correction and no inelastic radiative corrections were made. In Table XIV we list all the cross sections used for this analysis. The data with and without the elastic and quasielastic tails subtracted are plotted in Fig. 26. We have omitted points from further analysis when the radiative tail subtractions were greater than 25%, and we have made no inelastic radiative corrections for any of the targets. We should point out, however, that applying our procedure for calculating the inelastic radiative corrections to the data does not change the results of the comparison of cross sections between nuclei. In models such as vector dominance that show decreasing shadowing for small ω' , the effects of the radiation process tend to dilute the possible shadowing when looking at

data which are not radiatively corrected.³⁶ Comparisons with theoretical predictions, therefore, require the calculation of the expected results including the effects of the radiation process.

We calculate the "shadowing factor"

$$F = \frac{\sigma(A)}{N\sigma(D) - (N - Z)\sigma(H)}, \quad (35)$$

where $\sigma(D)$ and $\sigma(H)$ are the deuterium and hydrogen cross sections, N is the average number of neutrons, and Z the number of protons in the nucleus. No corrections for proton smearing were made to $\sigma(H)$, since it affects the value of F by $\leq 0.5\%$. In Fig. 27, F is plotted versus A for each of the kinematic points. The results for each (q^2, W) point were fitted to the expression

$$F = a_0 A^\epsilon, \quad (36)$$

determining the parameters a_0 and ϵ . (Note that in this section ϵ is not the photon polarization defined in Sec. III.) The results are listed in Table XV and ϵ is plotted as a function of x' in Fig. 28.

Systematic errors are difficult to estimate. Many sources of systematic error cause shifts in ϵ at all values of x' and are, therefore, "normalization" errors in ϵ . We estimate these kinds of errors as ± 0.02 in the value of ϵ .

The subtraction of elastic radiative tails introduces errors which would depend on x' (though the dependence is also a function of E_0). We are, therefore, reluctant to interpret the observed fall-off at low x' as definitive evidence for the observation of shadowing electroproduction.

V. CONCLUSION

The results of this experiment can be briefly summarized as follows:

(1) The turn-on of scaling behavior for the proton appears to take a remarkably simple form in q^2 , which is independent of the value of ω' chosen and is consistent with the closure approximation.

TABLE XIII. Electroproduction sum rules. Expected parton model values are from Ref. 33; $\langle N \rangle$ is the average number of partons. The extended range of $0.02 < x' < 0.82$ includes data σ_n/σ_p from Ref. 26. The errors are an estimate of the systematic uncertainty from the data.

	Expected		Measured values	
	3 quarks	Parton model	This experiment $0.02 < x' < 0.28$	Extended range $0.02 < x' < 0.82$
I_{1p}	$\frac{1}{3}$	$\frac{2}{9} + \frac{1}{3\langle N \rangle}$	0.089 ± 0.005	0.152 ± 0.009
$I_{1p} - I_{1n}$	$\frac{1}{9}$	$\frac{1}{3\langle N \rangle}$	0.019 ± 0.003	0.045 ± 0.005
I_{2p}	1	$\frac{1}{3} + \frac{2\langle N \rangle}{9}$	0.895 ± 0.072	1.052 ± 0.085
$I_{2p} - I_{2n}$	$\frac{1}{3}$	$\frac{1}{3}$	0.139 ± 0.031	0.200 ± 0.040

TABLE XIV. Cross sections for A -dependence analysis.

W (GeV)	Target	Raw ($\mu\text{b}/\text{GeV sr}$)	Raw-tails ($\mu\text{b}/\text{GeV sr}$)	W (GeV)	Target	Raw ($\mu\text{b}/\text{GeV sr}$)	Raw-tails ($\mu\text{b}/\text{GeV sr}$)
$E_0 = 13 \text{ GeV}$							
2.00	H	3.173 \pm 0.028	3.027 \pm 0.028	3.25	H	1.477 \pm 0.015	1.339 \pm 0.015
	D	5.697 \pm 0.068	5.490 \pm 0.068		D	2.628 \pm 0.017	2.449 \pm 0.017
	Be	25.24 \pm 0.39	24.39 \pm 0.39		Be	11.70 \pm 0.18	10.92 \pm 0.18
	Al	76.4 \pm 1.2	73.7 \pm 1.3		Al	34.82 \pm 0.46	31.94 \pm 0.46
	Cu	186.1 \pm 3.9	180.0 \pm 3.9		Cu	81.3 \pm 1.5	74.1 \pm 1.5
	Au	554. \pm 20.	538. \pm 20.		Au	270.1 \pm 8.8	247.7 \pm 8.8
2.25	H	2.651 \pm 0.029	2.525 \pm 0.029	3.50	H	1.307 \pm 0.014	1.140 \pm 0.014
	D	4.697 \pm 0.039	4.523 \pm 0.039		D	2.354 \pm 0.017	2.141 \pm 0.017
	Be	21.34 \pm 0.28	20.62 \pm 0.28		Be	10.28 \pm 0.14	9.34 \pm 0.14
	Al	64.32 \pm 0.92	62.04 \pm 0.92		Al	31.19 \pm 0.50	27.43 \pm 0.50
	Cu	156.8 \pm 2.6	151.6 \pm 2.6		Cu	73.7 \pm 1.4	63.6 \pm 1.4
	Au	481. \pm 15.	467. \pm 15.		Au	230.1 \pm 7.0	195.7 \pm 7.0
2.50	H	2.192 \pm 0.024	2.076 \pm 0.024	3.75	H	1.265 \pm 0.020	1.045 \pm 0.020
	D	3.946 \pm 0.034	3.788 \pm 0.034		D	2.185 \pm 0.031	1.912 \pm 0.031
	Be	18.11 \pm 0.25	17.45 \pm 0.25		Be	10.17 \pm 0.20	8.70 \pm 0.20
	Al	53.63 \pm 0.77	51.50 \pm 0.77		Al	29.66 \pm 0.62	24.29 \pm 0.62
	Cu	132.4 \pm 2.4	127.6 \pm 2.4		Cu	70.9 \pm 2.0	55.4 \pm 2.0
	Au	414. \pm 13.	401. \pm 13.		Au	223.1 \pm 8.4	164.3 \pm 8.4
2.75	H	1.890 \pm 0.018	1.774 \pm 0.018	4.00	H	1.221 \pm 0.022	
	D	3.414 \pm 0.021	3.259 \pm 0.021		D	2.135 \pm 0.035	
	Be	15.12 \pm 0.17	14.47 \pm 0.17		Be	9.35 \pm 0.23	
	Al	45.71 \pm 0.60	43.55 \pm 0.60		Al	29.72 \pm 0.72	
	Cu	106.2 \pm 1.7	101.2 \pm 1.7		Cu	74.3 \pm 2.5	
	Au	345.8 \pm 8.1	331.9 \pm 8.1		Au	241. \pm 11.	
3.00	H	1.639 \pm 0.016	1.517 \pm 0.016				
	D	2.960 \pm 0.018	2.798 \pm 0.018				
	Be	13.21 \pm 0.19	12.52 \pm 0.19				
	Al	39.76 \pm 0.52	37.36 \pm 0.52				
	Cu	92.3 \pm 1.7	86.6 \pm 1.7				
	Au	286.0 \pm 9.3	269.4 \pm 9.3				
$E_0 = 20 \text{ GeV}$							
2.50	H	0.762 \pm 0.007	0.753 \pm 0.007	3.00	H	0.634 \pm 0.007	0.625 \pm 0.007
	D	1.292 \pm 0.008	1.279 \pm 0.008		D	1.125 \pm 0.007	1.112 \pm 0.007
	Be	5.72 \pm 0.11	5.67 \pm 0.11		Be	5.119 \pm 0.070	5.061 \pm 0.070
	Al	17.66 \pm 0.34	17.48 \pm 0.34		Al	15.40 \pm 0.24	15.18 \pm 0.24
	Cu	42.44 \pm 0.95	42.03 \pm 0.95		Cu	36.51 \pm 0.79	36.02 \pm 0.79
	Au	123.5 \pm 5.5	122.3 \pm 5.5		Au	115.1 \pm 3.5	113.7 \pm 3.5
2.75	H	0.695 \pm 0.007	0.686 \pm 0.007	3.25	H	0.583 \pm 0.006	0.573 \pm 0.006
	D	1.205 \pm 0.006	1.192 \pm 0.006		D	1.038 \pm 0.007	1.023 \pm 0.007
	Be	5.39 \pm 0.11	5.34 \pm 0.11		Be	4.731 \pm 0.094	4.666 \pm 0.094
	Al	16.99 \pm 0.20	16.80 \pm 0.20		Al	14.70 \pm 0.22	14.43 \pm 0.22
	Cu	40.4 \pm 1.2	40.0 \pm 1.2		Cu	35.49 \pm 1.03	34.87 \pm 1.03
	Au	123.3 \pm 5.1	122.1 \pm 5.1		Au	112.7 \pm 4.5	111.0 \pm 4.5

TABLE XIV. (cont'd.)

W (GeV)	Target	Raw ($\mu\text{b}/\text{GeV sr}$)	Raw-tails ($\mu\text{b}/\text{GeV sr}$)	W (GeV)	Target	Raw ($\mu\text{b}/\text{GeV sr}$)	Raw-tails ($\mu\text{b}/\text{GeV sr}$)
$E_0 = 20 \text{ GeV}$							
3.50	H	0.532 ± 0.006	0.521 ± 0.006	4.75	H	0.424 ± 0.004	
	D	0.956 ± 0.006	0.940 ± 0.006		D	0.765 ± 0.006	
	Be	4.308 ± 0.059	4.232 ± 0.059		Be	3.392 ± 0.072	
	Al	13.04 ± 0.19	12.70 ± 0.19		Al	10.23 ± 0.16	
	Cu	31.44 ± 0.67	30.60 ± 0.67		Cu		
	Au	97.4 ± 3.0	95.0 ± 3.0		Au	76.6 ± 3.5	
3.75	H	0.495 ± 0.005	0.481 ± 0.005	5.00	H	0.458 ± 0.005	
	D	0.899 ± 0.007	0.880 ± 0.007		D	0.796 ± 0.007	
	Be	4.001 ± 0.080	3.908 ± 0.080		Be	3.591 ± 0.084	
	Al	12.49 ± 0.19	12.06 ± 0.19		Al	10.68 ± 0.17	
	Cu	30.06 ± 0.87	28.92 ± 0.87		Cu	25.94 ± 0.88	
	Au	90.7 ± 3.7	87.3 ± 3.7		Au	76.4 ± 4.1	
4.00	H	0.471 ± 0.004	0.454 ± 0.004	5.25	H	0.497 ± 0.007	
	D	0.840 ± 0.006	0.817 ± 0.006		D	0.903 ± 0.010	
	Be	3.796 ± 0.036	3.679 ± 0.036		Be	4.16 ± 0.11	
	Al	11.23 ± 0.17	10.67 ± 0.17		Al	12.87 ± 0.25	
	Cu	27.53 ± 0.59	25.98 ± 0.59		Cu	31.5 ± 1.2	
	Au	86.2 ± 2.6	81.3 ± 2.6		Au	117.1 ± 5.9	
4.25	H	0.431 ± 0.005	0.408 ± 0.005	5.50	H	0.601 ± 0.011	
	D	0.783 ± 0.010	0.752 ± 0.010		D	1.009 ± 0.013	
	Be	3.428 ± 0.072	3.275 ± 0.072		Be	4.79 ± 0.15	
	Al	10.67 ± 0.19	9.92 ± 0.19		Al	16.69 ± 0.39	
	Cu	26.32 ± 0.80	24.19 ± 0.80		Cu	46.5 ± 2.0	
	Au	86.0 ± 3.7	78.8 ± 3.7		Au	$186 \pm 11.$	
4.50	H	0.426 ± 0.004	0.394 ± 0.004				
	D	0.777 ± 0.006	0.735 ± 0.006				
	Be	3.385 ± 0.049	3.177 ± 0.049				
	Al	10.44 ± 0.17	9.42 ± 0.17				
	Cu	24.03 ± 0.50	21.02 ± 0.50				
	Au	69.8 ± 2.3	58.9 ± 2.3				

The lack of q^2 dependence in the ratio σ_D/σ_p^S suggest that the turn-on of scaling in the neutron is similar to that observed for the proton.

(2) The ratio of $\nu W_{zn}/\nu W_{zp}$ is less than unity even for ω' as large as 20, suggesting a sizable nondiffractive component to the scattering.

(3) We observe no significant resonance enhancements between $W=2 \text{ GeV}$ and $W=3 \text{ GeV}$.

(4) For our range of $q^2=0.1$ to $1.8 \text{ (GeV}/c)^2$ the first resonance decreases in size relative to its underlying background. For the higher-lying resonance enhancements the ratio of peak to background remains relatively constant, varying no more than 30% from $q^2=0$ to $q^2=1.8 \text{ (GeV}/c)^2$.

(5) Electroproduction shadowing in heavy nuclei is significantly smaller than in photoproduction.

ACKNOWLEDGMENTS

We would like to thank the operating crew of the SLAC accelerator for putting up with our requests for a very well-defined beam and producing one of the finest beams available. We also want to thank the Spectrometer Facilities Group, C. Sinclair and D. Sherden in particular, for assistance with the spectrometer magnet control and the detectors. The Cryogenics Group under J. Mark is also thanked for construction and keeping a watchful eye on the targets. We also thank R. Haley for programming assistance during the early stages of the run and analysis. Special appreciation is given to Connie Logg, who provided many of the programs for the final analysis, which will be

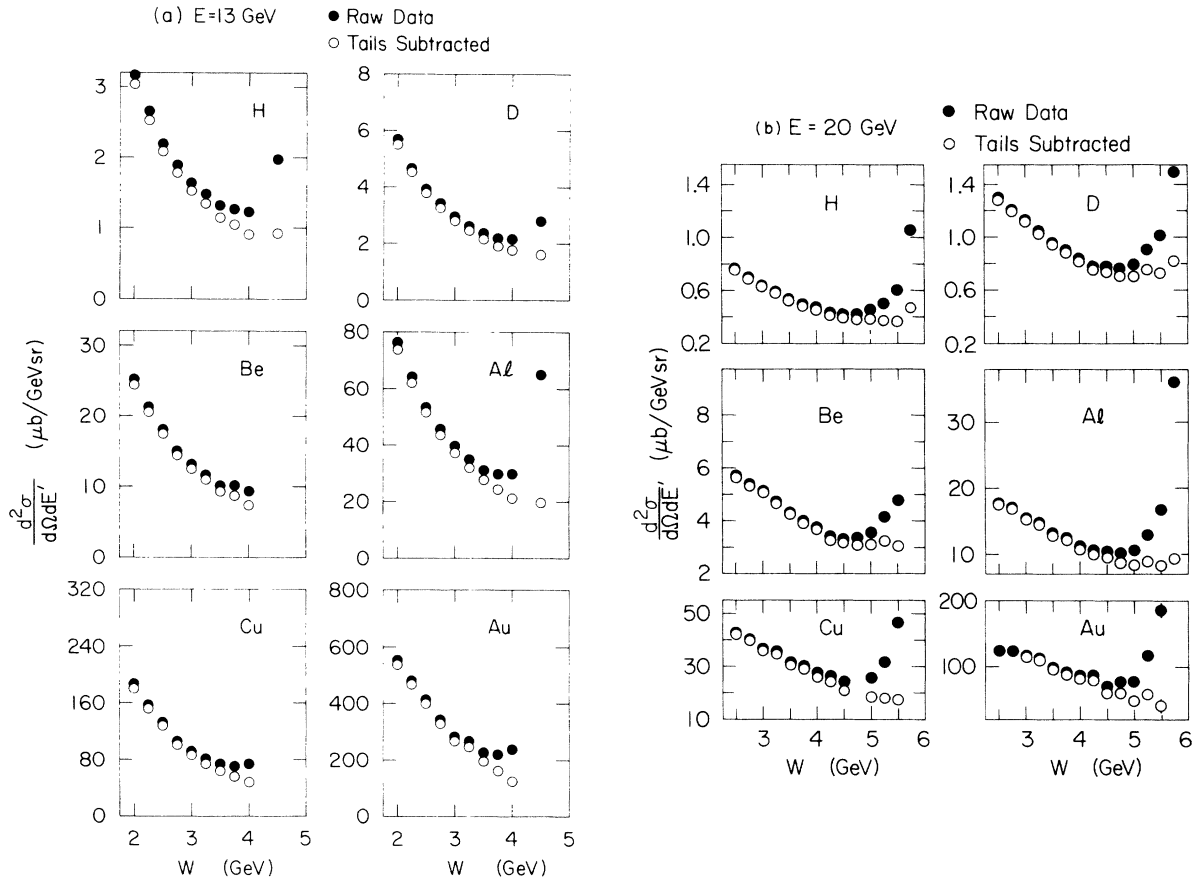


FIG. 26. Measured values of the cross section $d^2\sigma/d\Omega dE'$ vs W for each of the six targets as shown: (a) incident energy, $E_0=13$ GeV; (b) incident energy, $E_0=20$ GeV (note suppressed zeros). The closed circles are the data before any radiative corrections; the open circles are the data after elastic and quasielastic tails are subtracted. Statistical errors are shown where they are larger than the plotted points. Data where the subtraction arising from radiative corrections exceeds 25% are not used in the subsequent analysis.

useful for future electroproduction experiments at SLAC. For technical help and construction of the apparatus, we thank G. Johnson, K. Doty, and W. Weeks.

APPENDIX A: RADIATIVE CORRECTION FORMULAS

In this appendix we present the expressions used in the radiative corrections for this experiment. The corrections consisted of: the radiative tail from elastic scattering, $\sigma_{\text{el tail}}$; the tail from quasielastic scattering in the case of targets other than hydrogen, $\sigma_{\text{q tail}}$; and the inelastic radiative corrections. We are able to calculate exact radiative tails under the assumption of one-photon exchange and for single-photon emission.³⁷ This we call $\sigma_{\text{ex tail}}$. We also can use the angle-peaking approximation to calculate $\sigma_{\text{pk tail}}$, which is a faster calculation and is used where speed is more impor-

tant than accuracy. In the case of the quasielastic scattering, we must include the smearing due to the motion of the nucleons within the nucleus. Because of speed limitations we use the peaking approximation for radiation when the smearing calculation is done to get σ_{qt} . This is then corrected by comparing an unsmearred, but exact, radiation calculation to the unsmearred peaking approximation result. In both elastic and quasielastic cases, we correct for the finite solid angle of the detector using the peaking approximation to average over the acceptance to get σ_{finite} . By putting all these factors together, we obtain the following for the total elastic and quasielastic tails:

$$\sigma_{\text{el tail}} = \sigma_{\text{ex tail}} \frac{\sigma_{\text{finite}}}{\sigma_{\text{pk tail}}}, \quad (\text{A1})$$

$$\sigma_{\text{q tail}} = \sigma_{\text{qt}} \frac{\sigma_{\text{ex tail}}}{\sigma_{\text{pk tail}}} \frac{\sigma_{\text{finite}}}{\sigma_{\text{pk tail}}}. \quad (\text{A2})$$

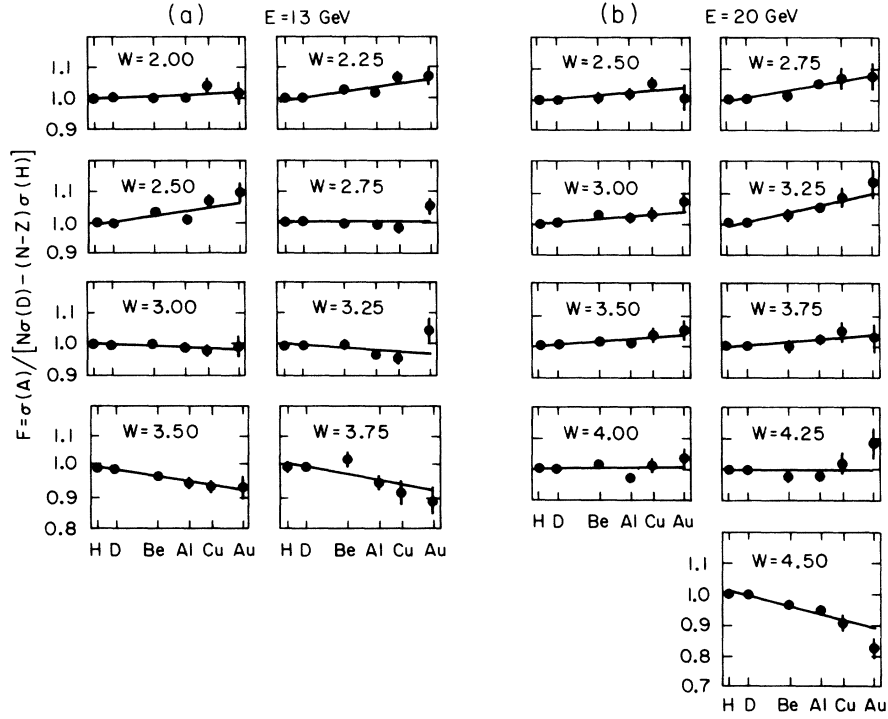


FIG. 27. The shadowing factor F (see text) vs A for each kinematic point. The lines are fits to the form $a_0 A^\epsilon$ for each plot. Only statistical errors are shown. (a) Incident energy, $E_0=13$ GeV; (b) incident energy, $E_0=20$ GeV.

TABLE XV. A -dependence results. Results of the fits to the A dependence of the form $F=a_0 A^\epsilon$. The errors shown are from the fit only. Systematic errors can shift the values of ϵ by as much as ± 0.02 .

E_0 (GeV)	W (GeV)	q^2 [(GeV/c) 2]	x'	ν (GeV)	a_0	$\epsilon \times 1000$	χ^2 (4 degrees of freedom)
13	2.00	0.695	0.148	2.034	0.998 ± 0.008	3.8 ± 3.8	2.1
	2.25	0.660	0.115	2.581	0.994 ± 0.008	12.9 ± 3.5	2.5
	2.50	0.621	0.090	3.191	0.994 ± 0.008	13.2 ± 3.7	5.7
	2.75	0.578	0.071	3.870	0.998 ± 0.006	0.5 ± 3.1	5.4
	3.00	0.531	0.056	4.612	1.002 ± 0.007	-3.0 ± 3.5	0.6
	3.25	0.481	0.044	5.416	1.003 ± 0.007	-6.2 ± 3.7	6.5
	3.50	0.425	0.034	6.282	1.007 ± 0.008	-15.4 ± 4.0	0.8
	3.75	0.366	0.025	7.216	1.014 ± 0.014	-18.8 ± 6.2	5.6
20	2.50	1.588	0.203	3.707	0.997 ± 0.006	7.2 ± 4.1	1.7
	2.75	1.524	0.168	4.373	0.991 ± 0.006	16.0 ± 3.7	1.7
	3.00	1.453	0.139	5.095	0.996 ± 0.006	9.0 ± 3.6	1.4
	3.25	1.375	0.115	5.894	0.990 ± 0.007	18.8 ± 4.1	1.8
	3.50	1.292	0.095	6.750	0.997 ± 0.007	6.4 ± 3.6	1.3
	3.75	1.203	0.079	7.666	0.997 ± 0.007	6.4 ± 4.3	0.9
	4.00	1.107	0.065	8.647	1.001 ± 0.007	0.8 ± 3.6	6.2
	4.25	1.005	0.053	9.692	0.997 ± 0.009	0.3 ± 5.0	4.9
	4.50	0.897	0.042	10.800	1.012 ± 0.007	-24.6 ± 4.0	7.3

In the case of the inelastic correction, we use the peaking approximation and a model for the inelastic cross sections as described in the text. The following are the formulas as used in the analysis:

1. General definitions

We first consider the cross section for elastic electron scattering from a target of mass M_T . This will define the structure functions $W_1^{e1}(q^2)$ and $W_2^{e1}(q^2)$:

$$\sigma_{e1} \equiv \left(\frac{d\sigma}{d\Omega} \right)_{e1} = \frac{\alpha^2 \cos^2(\frac{1}{2}\theta)}{4E_0^2 \sin^4(\frac{1}{2}\theta)} \frac{E'_{e1}}{E_0} \times [W_2^{e1} + 2 \tan^2(\frac{1}{2}\theta) W_1^{e1}], \quad (\text{A3})$$

where E_0 is the incident energy θ is the laboratory scattering angle and

$$E'_{e1} = \frac{E_0}{1 + (2E_0/M_T) \sin^2(\frac{1}{2}\theta)}, \quad (\text{A4})$$

α = fine-structure constant

$$\approx 1/137.03604.$$

We consider three cases, elastic proton scattering, elastic nucleus scattering, and quasielastic scattering, and define the parameters needed for the calculation:

(1) elastic electron-proton scattering:

$$M_T = M_p = 0.938256 \text{ GeV}, \quad (\text{A5})$$

$$W_1^{e1} = \tau G_{Mp}^2, \quad W_2^{e1} = \frac{G_{Ep}^2 + \tau G_{Mp}^2}{1 + \tau}, \quad (\text{A6})$$

where

$$\tau = q^2/4M_p^2,$$

$$G_{Mp} = (1 + K_p)G_{Ep}, \quad K_p = 1.7927,$$

and

$$G_{Ep} = P(q^2)/(1 + q^2/0.71)^2, \quad (\text{A7})$$

where $P(q^2)$ takes into account the deviation of the measured form factors from the dipole expression,¹² and is given by

$$P(q^2) = \sum_{i=0}^5 \left(H_i \prod_{\substack{j=0 \\ j \neq i}}^5 \{ [(q^2)^{1/2} - j]/(i - j) \} \right), \quad (\text{A8})$$

and $H_0 = 1.0007$, $H_1 = 1.01807$, $H_2 = 1.05584$, $H_3 = 0.836380$, $H_4 = 0.6864584$, $H_5 = 0.672830$;

(2) deuteron elastic:

$$M_T = 1.87537 \text{ GeV}, \quad (\text{A9})$$

$$W_1^{e1} = F_d^2 \tau G_S^2, \quad W_2^{e1} = F_d^2 (G_p^2 + \frac{2}{3} \tau G_S^2), \quad (\text{A10})$$

where²⁵

$$F_d = F(q)$$

$$= \frac{1.580}{q} \left(\tan^{-1} \frac{q}{0.930} - 2 \tan^{-1} \frac{q}{3.19} + \tan^{-1} \frac{q}{5.45} \right)$$

and

$$q = (q^2)^{1/2} \text{ in fm}^{-1}, \quad (\text{A11})$$

and³⁸

$$G_p = F_{1n} + F_{1p},$$

$$G_S = F_{1n} + F_{1p} + K_n F_{2n} + K_p F_{2p},$$

$$F_{1n} = \tau G_{Mn}/(1 + \tau),$$

$$F_{1p} = (G_{ep} + \tau G_{Mp})/(1 + \tau), \quad (\text{A12})$$

$$F_{2n} = G_{Mn}/K_n(1 + \tau),$$

$$F_{2p} = (G_{Mp} - G_{Ep})/[K_p(1 + \tau)],$$

$$G_{Mn} = K_n G_{Ep},$$

and

$$K_n = -1.91348;$$

(3) beryllium elastic

$$M_T = (0.938256/1.00797) \times 9.012$$

$$= 8.38871 \text{ GeV}, \quad (\text{A13})$$

$$W_1^{e1} = 0, \quad W_2^{e1} = [ZF(q)]^2, \quad (\text{A14})$$

where³⁹

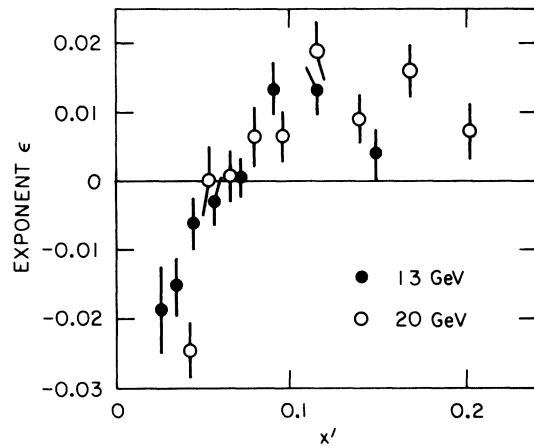


FIG. 28. The exponent ϵ from the fits to the shadowing factor $F = a_0 A^\epsilon$ vs x' . The closed circles are from the 13-GeV data, open circles from the 20-GeV data. Only statistical errors are shown in the figure. Systematic errors can shift the values of ϵ by as much as ± 0.02 .

$$F(q) = 1 - ax^2/[2k(2+3a)]e^{-x^2/4k}$$

and

$$k = 3(2+5a)/2(2+3a), \quad (\text{A15})$$

$$a = \frac{1}{3}(Z-2),$$

$$x = q \times 1.07A^{1/3},$$

$$q \text{ in fm}^{-1},$$

Z = atomic charge number of the nucleus and is given in Table I;

(4) aluminum, copper, and gold elastic:

$$\begin{aligned} M_T &= (0.938\,256/1.007\,97) \times 26.98, 63.54, 197 \\ &= 25.1140 \text{ GeV}, 59.1454 \text{ GeV}, 183.375 \text{ GeV}, \end{aligned} \quad (\text{A16})$$

$$W_1^{e1} = 0, \quad W_2^{e1} = [ZF(q)]^2, \quad (\text{A17})$$

where

$$\begin{aligned} F(q) &= (1 + \frac{1}{6}q^2c^2)^{-1} \exp(-\frac{1}{6}q^2b^2), \\ b &= 2.4 \text{ fm}, \\ c &= 1.07A^{1/3} \text{ fm}, \end{aligned} \quad (\text{A18})$$

and

$$q \text{ is in fm}^{-1};$$

(5) quasielastic:

$$M_T = 0.938\,256 \text{ GeV}, \quad (\text{A19})$$

$$W_1^{e1} = \tau G_M'^2, \quad W_2^{e1} = \frac{G_E'^2 + \tau G_M'^2}{1 + \tau}, \quad (\text{A20})$$

where¹⁵

$$\begin{aligned} G_E'^2 &= Z[1 - F^2(q)]G_{E_p}^2, \\ G_M'^2 &= [Z(1 + K_p)^2 + NK_n^2]G_{E_p}^2, \end{aligned} \quad (\text{A21})$$

and the appropriate $F(q)$ is chosen according to the target, and N = number of neutrons in the target and is given in Table I.

2. "Exact" radiative tail

The cross section σ_{ex} for the radiative tail from a state of definite mass M_f can be calculated exactly under the assumption of one-photon exchange and for single-photon emission. It depends upon knowledge of the structure functions $W_1^{e1}(q^2)$ and $W_2^{e1}(q^2)$ and is given by Tsai.¹³ We have changed the notation in the following sections from that used in the previous part of this paper, in order to follow more closely that used by Tsai. This means that now

$$\begin{aligned} s(E_s, \vec{s}): & \text{ four-momentum of the incident electron } (E_s = E_0), \\ p(E_p, \vec{p}): & \text{ four-momentum of the outgoing electron } (E_p = E'), \\ t(M_T, 0): & \text{ four-momentum of the target particle,} \\ k(\omega, \vec{k}): & \text{ four-momentum of the real photon emitted,} \end{aligned} \quad (\text{A22})$$

and in addition we define the four vectors

$$\begin{aligned} u &= s + t - p, \\ P_f &= u - k, \end{aligned} \quad (\text{A23})$$

where

$$P_f \cdot P_f = M_f^2.$$

For the radiative tail from elastic scattering $M_f = M_T$.

Then following Tsai we obtain

$$\begin{aligned} \sigma_{\text{ex}} &\equiv \left(\frac{d^2\sigma}{d\Omega dE_p} \right)_{\text{ex}} = \frac{\alpha^3}{(2\pi)} \left(\frac{E_p}{E_s} \right) \int_{-1}^1 \frac{2M_T \omega d(\cos\theta_k)}{q^4(u_0 - |\vec{u}| \cos\theta_k)} \\ &\times \left(\tilde{W}_2(q^2) \left\{ \frac{-am^2}{x^3} \left[2E_s(E_p + \omega) + \frac{q^2}{2} \right] - \frac{a'm^2}{y^3} \left[2E_p(E_s - \omega) + \frac{q^2}{2} \right] \right. \right. \\ &\quad - 2 + 2\nu(x^{-1} - y^{-1}) \{ m^2(s \cdot p - \omega^2) + (s \cdot p)[2E_s E_p - (s \cdot p) + \omega(E_s - E_p)] \} \\ &\quad + x^{-1} \left[2(E_s E_p + E_s \omega + E_p^2) + \frac{q^2}{2} - (s \cdot p) - m^2 \right] \\ &\quad \left. \left. - y^{-1} \left[2(E_s E_p - E_p \omega + E_s^2) + \frac{q^2}{2} - (s \cdot p) - m^2 \right] \right\} \right. \\ &\quad \left. + \tilde{W}_1(q^2) \left[\left(\frac{a}{x^3} + \frac{a'}{y^3} \right) m^2(2m^2 + q^2) + 4 + 4\nu(x^{-1} - y^{-1})(s \cdot p)(s \cdot p - 2m^2) \right. \right. \\ &\quad \left. \left. + (x^{-1} - y^{-1})(2s \cdot p + 2m^2 - q^2) \right] \right), \end{aligned} \quad (\text{A24})$$

where ω is the photon energy in the lab system

$$\omega = \frac{1}{2}(u^2 - M_T^2)/(u_0 - |\vec{u}| \cos \theta_k), \quad (\text{A25})$$

$$s \cdot p = E_s E_p - |\vec{p}| |\vec{s}| \cos \theta, \quad (\text{A26})$$

$$u_0 = E_s + M_T - E_p, \quad (\text{A27})$$

$$|\vec{u}| = (u_0^2 - u^2)^{1/2}, \quad (\text{A28})$$

$$u^2 = 2m^2 + M_T^2 - 2(s \cdot p) + 2M_T(E_s - E_p), \quad (\text{A29})$$

$$q^2 = 2m^2 - 2(s \cdot p) - 2\omega(E_s - E_p) + 2\omega|\vec{u}| \cos \theta_k, \quad (\text{A30})$$

$$a = \omega(E_p - |\vec{p}| \cos \theta_p \cos \theta_k), \quad (\text{A31})$$

$$a' = \omega(E_s - |\vec{s}| \cos \theta_s \cos \theta_k), \quad (\text{A32})$$

$$b' = -\omega|\vec{p}| \sin \theta_p \sin \theta_k, \quad (\text{A33})$$

$$v = (a' - a)^{-1}, \quad (\text{A34})$$

$$\cos \theta_p = \frac{|\vec{s}| \cos \theta - |\vec{p}|}{|\vec{u}|}, \quad (\text{A35})$$

$$\cos \theta_s = \frac{|\vec{s}| - |\vec{p}| \cos \theta}{|\vec{u}|}, \quad (\text{A36})$$

$$x = (a^2 - b'^2)^{1/2}, \quad (\text{A37})$$

$$y = (a'^2 - b'^2)^{1/2}, \quad (\text{A38})$$

$$m = \text{electron mass} \\ = 0.511 \text{ MeV}, \quad (\text{A39})$$

$$\theta = \text{scattering angle}, \quad (\text{A40})$$

$$\theta_k = \text{angle between } \vec{u} \text{ and } \vec{k}, \quad (\text{A41})$$

and

$$\tilde{W}_1(q^2) = \tilde{F}(q^2) W_1^{\text{el}}(q^2), \quad (\text{A42})$$

$$\tilde{W}_2(q^2) = \tilde{F}(q^2) W_2^{\text{el}}(q^2), \quad (\text{A43})$$

$$\tilde{F}(q^2) = 1 + 0.5772 \times bT + \frac{2\alpha}{\pi} \left[\frac{-14}{9} + \frac{13}{12} \ln \frac{-q^2}{m^2} \right] \\ - \frac{\alpha}{2\pi} \ln^2 \left(\frac{E_s}{E_p} \right) + \frac{\alpha}{\pi} \left[\frac{1}{6} \pi^2 - \Phi \left(\cos^2 \frac{\theta}{2} \right) \right], \quad (\text{A44})$$

$$b = \frac{4}{3} \left\{ 1 + \frac{1}{9} [(Z+1)/(Z+\eta)] [\ln(183Z^{-1/3}) - 1] \right\} \\ \approx 1.357, \quad (\text{A45})$$

$$\eta = \ln(1440Z^{-2/3})/\ln(183Z^{-1/3}), \quad (\text{A46})$$

$$T = t_a + t_b, \quad (\text{A47})$$

and t_b and t_a = total path length in units of radiation length of the electron in the target before and after the scattering, respectively (see Table II).

The Spence function is defined as

$$\Phi(x) = \int_0^x \frac{-\ln|1-y|}{y} dy. \quad (\text{A48})$$

3. Real bremsstrahlung and ionization loss in target

The straggling caused by target bremsstrahlung and ionization loss also contributes to the radiative tail and can be written

$$\sigma_b \equiv \left(\frac{d^2\sigma}{d\Omega dE_p} \right)_b \\ = \frac{M_T + 2(E_s - \omega_s) \sin^2(\frac{1}{2}\theta)}{M_T - 2E_p \sin^2(\frac{1}{2}\theta)} \\ \times \bar{\sigma}_{\text{el}}(E_s - \omega_s) \left[\frac{bt_b}{\omega_s} \phi(v_s) + \frac{\xi}{2\omega_s^2} \right] \\ + \bar{\sigma}_{\text{el}}(E_s) \left[\frac{bt_a}{\omega_p} \phi(v_p) + \frac{\xi}{2\omega_p^2} \right], \quad (\text{A49})$$

where

$$\omega_s = E_s - \frac{E_p}{1 - (2E_p/M_T) \sin^2(\frac{1}{2}\theta)}, \quad (\text{A50})$$

$$\omega_p = \frac{E_s}{1 + (2E_s/M_T) \sin^2(\frac{1}{2}\theta)} - E_p, \quad (\text{A51})$$

$$\xi = \frac{\pi m}{2\alpha} \frac{t_a + t_b}{(Z+\eta) \ln(183/Z^{1/3})}, \quad (\text{A52})$$

$$v_s = \omega_s/E_s, \quad (\text{A53})$$

$$v_p = \omega_p/(E_p + \omega_p),$$

$$\phi(v) = 1 - v + \frac{3}{4} v^2, \quad (\text{A54})$$

and

$$\bar{\sigma}_{\text{el}}(E) = \tilde{F}(q^2) \sigma_{\text{el}}(E). \quad (\text{A55})$$

4. Peaking approximation

It is also possible to develop an angle-peaking approximation for the exact radiative tail which looks very similar to the expression for target straggling:

$$\sigma_p \equiv \left(\frac{d^2\sigma}{d\Omega dE_p} \right)_{\text{peak approx.}} \\ = \frac{M_T + 2(E_s - \omega_s) \sin^2(\frac{1}{2}\theta)}{M_T - 2E_p \sin^2(\frac{1}{2}\theta)} \bar{\sigma}_{\text{el}}(E_s - \omega_s) \left[\frac{bt_r \phi(v_s)}{\omega_s} \right] \\ + \bar{\sigma}_{\text{el}}(E_s) \left[\frac{bt_r \phi(v_p)}{\omega_p} \right], \quad (\text{A56})$$

where

$$t_r = b^{-1}(\alpha/\pi) [\ln(-q^2/m^2) - 1]. \quad (\text{A57})$$

5. Multiple-photon correction

The cross section for single-photon emission is corrected for multiple-soft-photon radiation by multiplying by the factor

$$F_{\text{soft}} = \left(\frac{\omega_s}{E_s} \right)^{b(t_b+t_r)} \left(\frac{\omega_p}{E_p+\omega_p} \right)^{b(t_a+t_r)}. \quad (\text{A58})$$

6. Target radiation

In an attempt to take into account radiation from the target, we have used the approach in Ref. 12. We calculate the quantity

$$t = \sum_{i,j} \frac{\alpha}{\pi} \int \frac{k^2 d\Omega_k}{4\pi} Z_i Z_j \theta_i \theta_j \frac{(p_i p_j)}{(p_i k)(p_j k)} \quad (\text{A59})$$

where for

$i = 1$	$Z_i = -1$	$\theta_i = +1$	$p_i = s$
2	$+1$	$+1$	t
3	-1	-1	p
4	$+1$	-1	p_f

(A60)

and compare this to t_{el} , which is obtained by summing over only terms with i or $j = 1$ and 3. This results in a correction

$$R_t = t/t_{\text{el}}. \quad (\text{A61})$$

7. Complete elastic radiative tail

By putting all the above expressions together, we arrive at two expressions for the elastic tail: $\sigma_{\text{ex tail}}$, using the exact one-photon formula, and $\sigma_{\text{pk tail}}$, using the peaking approximation:

$$\sigma_{\text{ex tail}} = (\sigma_{\text{ex}} \cdot R_t + \sigma_b) F_{\text{soft}}, \quad (\text{A62})$$

$$\sigma_{\text{pk tail}} = (\sigma_p + \sigma_b) F_{\text{soft}}. \quad (\text{A63})$$

We also evaluate one other cross section using the peaking approximation, but averaging over the finite $\Delta\Omega$ acceptance of the spectrometer. This is done by summing over the individual θ and ϕ bins of the spectrometer:

$$\sigma_{\text{finite}} = \frac{1}{(2n_\theta + 1)(2n_\phi + 1)} \times \sum_{i=-n_\theta}^{n_\theta} \sum_{j=-n_\phi}^{n_\phi} \sigma_{\text{pk tail}}(E_s, E_1, \sin^2(\frac{1}{2}\theta)), \quad (\text{A64})$$

$$\sigma_q \equiv \left(\frac{d^2\sigma}{d\Omega dE_p} \right)_{\text{quasi}} \equiv \frac{\alpha^2 \cos^2(\frac{1}{2}\theta)}{4E_s^2 \sin^4(\frac{1}{2}\theta)} M_p \frac{P_{\text{c.m.}}}{2W_t}$$

$$\times \left\{ W_2^{\text{el}} \int_{-1}^{+1} \left[\mathfrak{F} + \frac{P_x^2}{M_p^2} 2 \tan^2(\frac{1}{2}\theta) \right] F_p E_{sp} d(\cos \theta_{\text{c.m.}}) + 2 \tan^2(\frac{1}{2}\theta) W_1^{\text{el}} \int_{-1}^{+1} F_p E_{sp} d(\cos \theta_{\text{c.m.}}) \right\}, \quad (\text{A69})$$

where

$$\sin^2(\frac{1}{2}\theta) = \sin^2\left(\frac{\theta_0 + i\Delta\theta}{2}\right) + \sin^2\left(\frac{j\Delta\phi}{2}\right) - 2 \sin^2\left(\frac{\theta_0 + i\Delta\theta}{2}\right) \sin^2\left(\frac{j\Delta\phi}{2}\right) \quad (\text{A65})$$

and

$$E_1 = \frac{E_s}{1 + 2(E_s/M_T) \sin^2(\frac{1}{2}\theta)} - \frac{E_s}{1 + 2(E_s/M_T) \sin^2(\frac{1}{2}\theta_0)} + E_p, \quad (\text{A66})$$

θ = scattering angle corresponding to the center of the θ - ϕ bin,

$\Delta\theta$ = width of θ bin,

$(2n_\theta + 1)$ = number of θ bins summed over, (A67)

θ_0 = central horizontal projected angle of the spectrometer,

$\Delta\phi$ = width of ϕ bin,

$(2n_\phi + 1)$ = number of ϕ bins summed over.

The final expression we have used for the complete elastic tail is then

$$\sigma_{\text{el tail}} = \sigma_{\text{ex tail}} \frac{\sigma_{\text{finite}}}{\sigma_{\text{pk tail}}}. \quad (\text{A68})$$

8. Quasielastic scattering

The quasielastic scattering cross section in Appendix A 1 does not take into account the motion of the nucleons within the nucleus. It represents a δ -function scattering with the correct total strength, but without the shape which is a result of smearing by the nuclear motion. Following the treatment by Atwood and West,¹⁴ we calculate the quasielastic peak cross section as

where W_1^{el} and W_2^{el} are the nucleon form factors as in Appendix A 1,

c.m. = center of mass of photon-deuteron system,

$$(A70)$$

$$P_{\text{c.m.}} = (E_{\text{c.m.}}^2 - M_n^2)^{1/2}, \quad (A71)$$

$$E_{\text{c.m.}} = (S_t + M_n^2 - M_p^2)/2W_t, \quad (A72)$$

$$W_t = S_t^{1/2}, \quad (A73)$$

$$S_t = M_d^2 + 2M_d\nu - q^2, \quad \nu = E_s - E_p, \quad |\vec{q}|^2 = q^2 + \nu^2, \quad (A74)$$

M_p = proton rest mass,

M_n = neutron rest mass,

M_d = deuteron rest mass, (A75)

$$\mathfrak{F} = \frac{1}{M_p^2} \left[\left(P^0 - \frac{\nu}{|\vec{q}|} P_z \right)^2 + \left(1 - \frac{\nu^2}{|\vec{q}|^2} \right) P_x^2 \right], \quad (A76)$$

and F_p = the probability that the nucleons have the momentum \vec{P}_{sp} inside the deuteron. We use $F_p = |\psi(\vec{P}_{sp})|^2$, where $\psi(\vec{P}_{sp})$ is the Fourier transform of the nonrelativistic spatial wave function.⁴⁰ In addition,

$$P_{sp}^2 = [E_{\text{c.m.}}|\vec{q}| - (M_d - \nu)P_{\text{c.m.}}\cos\theta_{\text{c.m.}}]^2/S_t, \quad (A77)$$

$$E_{sp}^2 = P_{sp}^2 + (M_p^2 \text{ or } M_n^2), \quad (A78)$$

$$P^0 = M_d - E_{sp}, \quad (A79)$$

$$P_x^2 = \frac{1}{2}P_{\text{c.m.}}^2(1 - \cos^2\theta_{\text{c.m.}}), \quad (A80)$$

$$P_d^2 = P_{sp}^2 - 2P_x^2. \quad (A81)$$

9. Quasielastic radiative tail

The radiative tail associated with this quasielastic scattering is then calculated using the peaking approximation as given in the following formula:

$$\begin{aligned} \sigma_{\text{qt}} \equiv \left(\frac{d^2\sigma}{d\Omega dE_p} \right)_q &= \left(\frac{R\Delta E}{E_s} \right)^{b(t_b+t_r)} \left(\frac{\Delta E}{E_p} \right)^{b(t_a+t_r)} \left[1 - \frac{\xi/\Delta E}{1 - b(t_a+t_b+2t_r)} \right] \bar{\sigma}_q(E_s, E_p) \\ &+ \int_{E_s - R\Delta E}^{E_s} \bar{\sigma}_q(E'_s, E_p) \left(\frac{E_s - E'_s}{E_p R} \right)^{b(t_a+t_r)} \left(\frac{E_s - E'_s}{E_s} \right)^{b(t_b+t_r)} \left[\frac{b(t_b+t_r)}{E_s - E'_s} \phi \left(\frac{E_s - E'_s}{E_s} \right) + \frac{\xi}{2(E_s - E'_s)^2} \right] dE'_s \\ &+ \int_{E_p + \Delta E}^{E_p} \bar{\sigma}_q(E_s, E'_p) \left(\frac{E'_p - E_p}{E'_p} \right)^{b(t_a+t_r)} \left[\frac{(E'_p - E_p)R}{E_s} \right]^{b(t_b+t_r)} \left[\frac{b(t_a+t_r)}{E'_p - E_p} \phi \left(\frac{E'_p - E_p}{E'_p} \right) + \frac{\xi}{2(E'_p - E_p)^2} \right] dE'_p, \end{aligned} \quad (A82)$$

where

$$R = \frac{M_T + 2E_s \sin^2(\frac{1}{2}\theta)}{M_T - 2E_p \sin^2(\frac{1}{2}\theta)}, \quad \Delta E = 5 \text{ MeV}, \quad \phi(v) = 1 - v + \frac{3}{4}v^2, \quad \bar{\sigma}(E_s, E_p) = \bar{F}(q^2)\sigma_q(E_s, E_p). \quad (A83)$$

10. Inelastic radiative corrections

The corrections for radiation from the inelastic states is done in the peaking approximation.

By replacing σ_q in Appendix A 9 by a model for the inelastic cross section σ^M , we obtain the cross section with radiative effects included: $\sigma^M(\text{radiated})$. The measured cross sections are corrected by the ratio $\sigma^M(\text{radiated})/\sigma^M$.

APPENDIX B: NONRELATIVISTIC DERIVATION OF CLOSURE

1. General

We write the cross section $d\sigma/d\Omega$ for the scattering of a spinless particle interacting solely by Coulomb interaction as

$$d\sigma/d\Omega = \sigma_M G(q^2),$$

where σ_M is the Mott cross section. We will not worry about recoil factors. If the target is made up of N constituents with charge e_i each, then the form factor for the transition to a particular final state $\langle f |$ is given in the nonrelativistic Born approximation by

$$G_{0-f}(q^2) = \left| \sum_{i=1}^N e_i \langle f | e^{i\vec{q}\cdot\vec{R}_i} | 0 \rangle \right|^2, \quad (B1)$$

where \vec{R}_i is th position of the i th constituent. We shall distinguish the case where f is the same as the initial state (elastic scattering) from all others (inelastic scattering) and write

$$\begin{aligned} G_{\text{tot}}(q^2) &= \sum_f G_{0-f}(q^2) \\ &= G_{\text{el}}(q^2) + G_{\text{inel}}(q^2). \end{aligned} \quad (B2)$$

For the case of elastic scattering, $\langle f | = \langle 0 |$, so

$$G_{e1}(q^2) \equiv G_{0-0}(q^2) = \left| \sum_{i=1}^N e_i \langle 0 | e^{i\vec{q} \cdot \vec{R}_i} | 0 \rangle \right|^2. \quad (\text{B3})$$

For simplicity we assume that the ground-state expectation value is independent of the index i , that is, each constituent has the same momentum distribution inside the target, and define

$$F_{e1}(q^2) = \langle 0 | e^{i\vec{q} \cdot \vec{R}} | 0 \rangle. \quad (\text{B4})$$

Then, we get

$$G_{e1}(q^2) = \left| \sum_{i=1}^N e_i \right|^2 |F_{e1}(q^2)|^2. \quad (\text{B5})$$

Now, we evaluate the form factor for the total cross section:

$$\begin{aligned} G_{\text{tot}}(q^2) &= \sum_f G_{0-f}(q^2) \\ &= \sum_f \left| \sum_{i=1}^N e_i \langle f | e^{i\vec{q} \cdot \vec{R}_i} | 0 \rangle \right|^2. \end{aligned} \quad (\text{B6})$$

Expanding the squared matrix element,

$$\begin{aligned} G_{\text{tot}}(q^2) &= \sum_f \sum_{i,j} \sum_{\underline{1}} e_i e_j \langle 0 | e^{-i\vec{q} \cdot \vec{R}_j} | f \rangle \\ &\quad \times \langle f | e^{i\vec{q} \cdot \vec{R}_i} | 0 \rangle. \end{aligned} \quad (\text{B7})$$

We now make the closure approximation, that $\sum_f |f\rangle\langle f| = 1$. This assumes that all possible final states can be excited. So,

$$G_{\text{tot}}(q^2) = \sum_{i,j} \sum_{\underline{1}} e_i e_j \langle 0 | e^{i\vec{q} \cdot (\vec{R}_i - \vec{R}_j)} | 0 \rangle. \quad (\text{B8})$$

Separating out the diagonal terms and using the normalization $\langle 0 | 0 \rangle = 1$, yields

$$\begin{aligned} G_{\text{tot}}(q^2) &= \sum_{i=1}^N e_i^2 \\ &\quad + \sum_{i \neq j}^N e_i e_j \langle 0 | e^{i\vec{q} \cdot (\vec{R}_i - \vec{R}_j)} | 0 \rangle. \end{aligned} \quad (\text{B9})$$

Next, we separate out a contribution, $C(q^2)$, which vanishes if there are no two-particle correlations in the ground state and which we assume to be independent of the constituents' indices i and j so that

$$\langle 0 | e^{i\vec{q} \cdot (\vec{R}_i - \vec{R}_j)} | 0 \rangle = |F_{e1}(q^2)|^2 + C(q^2). \quad (\text{B10})$$

So,

$$\begin{aligned} G_{\text{tot}}(q^2) &= \sum_{i=1}^N e_i^2 + \sum_{i \neq j}^N e_i e_j |F_{e1}(q^2)|^2 \\ &\quad + C(q^2) \sum_{i \neq j}^N e_i e_j. \end{aligned} \quad (\text{B11})$$

Now, we can subtract the elastic contribution to get just the inelastic form factor:

$$\begin{aligned} G_{\text{inel}}(q^2) &= \sum_{i=1}^N e_i^2 + \sum_{i \neq j}^N e_i e_j |F_{e1}(q^2)|^2 \\ &\quad - \left| \sum_{i=1}^N e_i \right|^2 |F_{e1}(q^2)|^2 + C(q^2) \sum_{i \neq j}^N e_i e_j. \end{aligned} \quad (\text{B12})$$

Rewriting the second term containing F_{e1} as $\sum_{i,j}^N e_i e_j |F_{e1}(q^2)|^2$ yields

$$\begin{aligned} G_{\text{inel}}(q^2) &= \sum_{i=1}^N e_i^2 - \sum_{i=1}^N e_i^2 |F_{e1}(q^2)|^2 \\ &\quad + C(q^2) \sum_{i \neq j}^N e_i e_j \end{aligned} \quad (\text{B13})$$

or, summarizing the results;

$$G_{e1}(q^2) = \left| \sum_{i=1}^N e_i \right|^2 |F_{e1}(q^2)|^2, \quad (\text{B14})$$

$$\begin{aligned} G_{\text{inel}}(q^2) &= \sum_{i=1}^N e_i^2 [1 - |F_{e1}(q^2)|^2] \\ &\quad + C(q^2) \sum_{i \neq j}^N e_i e_j. \end{aligned}$$

2. Application

We can now apply these results to the proton and neutron if we consider them as being made of constituents. These yield immediately

$$\begin{aligned} \int_{\text{inel}} d\nu W_{2p}(q^2, \nu) &= \left(\sum_{i=1}^N e_i^2 \right)_p [1 - |F_{e1}^p(q^2)|^2] \\ &\quad + C_p(q^2) \left(\sum_{i \neq j}^N e_i e_j \right)_p, \end{aligned} \quad (\text{B15})$$

$$\begin{aligned} \int_{\text{inel}} d\nu W_{2n}(q^2, \nu) &= \left(\sum_{i=1}^N e_i^2 \right)_n [1 - |F_{e1}^n(q^2)|^2] \\ &\quad + C_n(q^2) \left(\sum_{i \neq j}^N e_i e_j \right)_n. \end{aligned} \quad (\text{B16})$$

F_{e1}^p and F_{e1}^n would be equal if the momentum distributions of the constituents were the same in the proton and neutron, so if the correlation terms were negligible, one might expect W_{2n}/W_{2p} to scale to lower values of q^2 than either W_{2p} or W_{2n} alone. Gottfried noted that in the simple quark model the charge sum in the correlation contribution vanishes for the proton, but not for the neutron.²⁷

For the case of particles with spin, magnetic moments, and more realistic ground states, the results get much more complicated. There are several more detailed accounts in the case of nuclear scattering in the literature.⁴¹ However, the simple approach stated here agrees with the spirit of the more complex analyses.

- *Work supported by the U. S. Atomic Energy Commission.
 †Present address: CERN, 1211 Geneva 23, Switzerland.
 ‡Present address: I. Physikalisches Institut, RWTH Aachen, Aachen, West Germany.
 §Present address: University of Wuppertal, Hofkamp 82-84, Wuppertal, West Germany.
 || Present address: Cornell University, Ithaca, New York, 14853.
- ¹E. D. Bloom *et al.*, Phys. Rev. Lett. 23, 930 (1969); M. Breidenbach *et al.*, 23, 935 (1969).
²J. D. Bjorken, Phys. Rev. 179, 1547 (1969).
³D. O. Caldwell *et al.*, Phys. Rev. D 7, 1362 (1973); V. Heynen *et al.*, Phys. Lett. 34B, 651 (1971); G. R. Brookes *et al.*, Phys. Rev. D 8, 2826 (1973).
⁴W. R. Ditzler, MIT thesis, 1971 (unpublished). See also H. Kendall, in *Proceedings of the 1971 International Symposium on Electron and Photon Interactions at High Energies*, edited by N. B. Mistry (Laboratory of Nuclear Studies, Cornell University, Ithaca, New York, 1972), p. 254, and J. Bailey *et al.*, Paper No. 295, submitted to XVII International Conference on High Energy Physics, London, 1974 (unpublished).
⁵See H. Kendall, in *Proceedings of the 1971 International Symposium on Electron and Photon Interactions at High Energies*, edited by N. B. Mistry (Laboratory of Nuclear Studies, Cornell University, Ithaca, New York 1971), p. 250, and R. Wilson, *ibid.*, p. 106. See also Bloom *et al.*, Phys. Rev. Lett. 30, 1186 (1973).
⁶R. S. Larsen and D. Horelick, SLAC, Report No. SLAC-PUB-398, 1968 (unpublished).
⁷Densities and radiation lengths were taken from Particle Data Group, Phys. Lett. 50B, 1 (1974).
⁸A. Bodek, Nucl. Instrum. Methods 109, 603 (1973).
⁹W. K. H. Panofsky, SLAC Report No. SLAC-PUB-798, review talk presented at the High Energy Physics Instrumentation Conference, Dubna, USSR, 1970 (unpublished).
¹⁰E. Bloom *et al.*, Nucl. Instrum. Methods 99, 255 (1972).
¹¹A. Boyarski *et al.*, Phys. Rev. Lett. 25, 695 (1970).
¹²G. Miller, thesis, Stanford University, 1970 available as Report No. SLAC-129 (unpublished).
¹³L. W. Mo and Y. S. Tsai, Rev. Mod. Phys. 41, 205 (1969); Y. S. Tsai, Report No. SLAC-PUB-848, Stanford Linear Accelerator Center, 1971 (unpublished).
¹⁴W. B. Atwood and G. B. West, Phys. Rev. D 7, 773 (1973).
¹⁵V. Z. Jankus, Phys. Rev. 102, 1586 (1956).
^{15a}See NAPS document No. 02710 for this table (13 pages). Order from ASIS/NAPS c/o Microfiche Publications, 440 Park Avenue South, New York, N. Y. 10016. Remit in advance. Make checks payable to Microfiche Publications. Photocopies are \$5.00. Microfiche are \$1.50. Outside of the United States and Canada, postage is \$2.00 for a photocopy or \$.50 for a fiche.
- ¹⁶L. A. Weber *et al.*, Cryogenics 2, 236 (1962).
¹⁷A. M. Roder *et al.*, Cryogenics 2, 16 (1963); BNL Cryogenic Data Handbook.
¹⁸S. J. Brodsky and J. Pumplin, Phys. Rev. 182, 5 (1969).
¹⁹E. D. Bloom and F. J. Gilman, Phys. Rev. Lett. 25, 1140 (1970).
²⁰S. D. Drell and J. D. Walecka, Ann. Phys. (N.Y.) 28, 18 (1964).
²¹L. N. Hand, Phys. Rev. 129, 1834 (1963).
²²B. Dudelzak, Orsay thesis, 1965 (unpublished); Ch. Berger *et al.*, Phys. Lett. 35B, 87 (1971); W. Bartel *et al.*, Nucl. Phys. B58, 429 (1973).
²³M. N. Rosenbluth, Phys. Rev. 79, 615 (1950).
²⁴J. S. Poucher *et al.*, Phys. Rev. Lett. 32, 118 (1974).
²⁵J. A. McIntyre, Phys. Rev. 103, 1464 (1956).
²⁶A. Bodek, Ph. D. thesis, Massachusetts Institute of Technology, MIT Laboratory for Nuclear Science Report No. COO-3069-116, 1972 (unpublished).
²⁷K. Gottfried, Phys. Rev. Lett. 18, 1174 (1967).
²⁸R. L. Walker, Phys. Rev. 182, 1729 (1969).
²⁹E. M. Riordan, Ph. D. Thesis, Massachusetts Institute of Technology, MIT Laboratory for Nuclear Science Report No. COO-3069-176, 1973 (unpublished).
³⁰H. Meyer *et al.*, Phys. Lett. 33B, 189 (1970); D. O. Caldwell *et al.*, Phys. Rev. Lett. 25, 609 (1970); T. A. Armstrong *et al.*, Phys. Rev. D 5, 1640 (1972).
³¹W. Bartel *et al.*, Phys. Lett. 28B, 148 (1968).
³²C. Callan and D. Gross, Phys. Rev. Lett. 21, 311 (1968).
³³J. D. Bjorken and E. A. Paschos, Phys. Rev. 185, 1975 (1969).
³⁴E. D. Bloom, in *Proceedings of the Sixth International Symposium on Electron and Photon Interactions at High Energies*, edited by H. Rollnik and W. Pfeil (North-Holland, Amsterdam, 1974), p. 227.
³⁵G. Bellettini *et al.*, Nucl. Phys. 79, 609 (1966).
³⁶D. Yennie, private communication.
³⁷Y. S. Tsai, in *Proceedings of the International Conference on Nuclear Structure, 1963* (Stanford Univ. Press, Stanford, California 1964), p. 221.
³⁸N. K. Glendenning and G. Kramer, Phys. Rev. 126, 2159 (1962).
³⁹This and the other heavy target form-factors are taken from R. Hofstadter, Annu. Rev. Nucl. Sci. 7, 231 (1957).
⁴⁰R. V. Reid, Jr., Ann. Phys. (N.Y.) 50, 411 (1968).
⁴¹For more detailed treatment of closure, see, for example O. Kofoed-Hanson and C. Wilkin, Ann. Phys. (N.Y.) 63, 309 (1971); K. W. McVoy and L. Van Hove, Phys. Rev. 125, 1034 (1962).

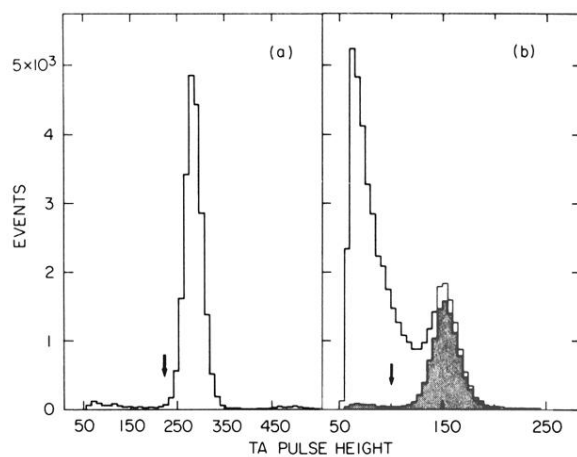


FIG. 4. Event distribution in the pulse height from the TA counter. The arrow indicates the position of the TA pulse-height cut. The lack of events below channel 50 is due to the discriminator threshold setting. Zero pulse height should typically appear near channel 40. (a) Typical running conditions, $E_0 = 13$ GeV, $E' = 9.13$ GeV. The peak shows the clean electron signal; a very small two-electron peak can be seen around channel 475. (b) One of the worst conditions, $E_0 = 20$ GeV, $E' = 4.14$ GeV. The shaded region shows the data after a cut on the pulse height from the Čerenkov counter is made.

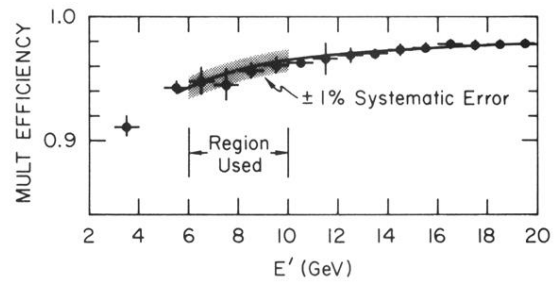


FIG. 5. Measured efficiency of the MULT pulse-height cut as a function of detected particle energy. The curve is the function used to correct the data in the region shown. The data points show the mean and standard deviation of all measurements from runs in each bin of E' .